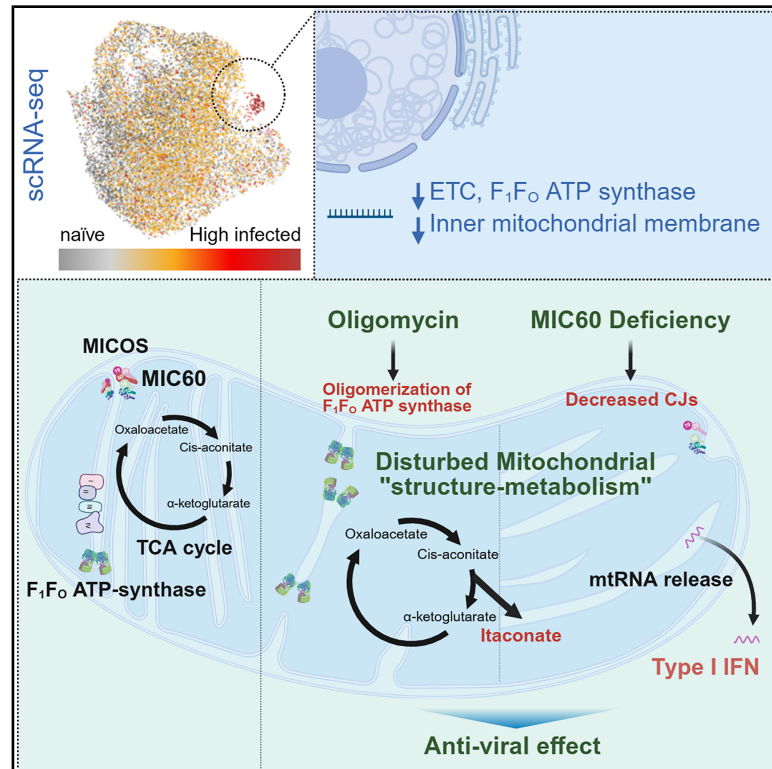


# Controlling mitochondrial membrane architecture via MIC60 determines viral replication to promote anti-viral immunity

## Graphical abstract



## Authors

Ichiro Katahira, Nina Liebrand, Michal Gorzkiewicz, ..., Ulrich Kalinke, Andreas S. Reichert, Philipp A. Lang

## Correspondence

langp@uni-duesseldorf.de

## In brief

Katahira et al. show scRNA-seq indicating roles of mitochondrial membrane architecture during VSV infection. Altered mitochondrial structure-metabolism by F<sub>1</sub>F<sub>0</sub> ATP synthase inhibition, inducing oligomerization of the complex, reduces viral replication. Consistently, MIC60 deletion in CD11c-expressing cells limits viral replication and consequently reduces prolonged immune activation, associated with accumulation of anti-viral itaconate.

## Highlights

- scRNA-seq suggests involvement of mitochondrial architecture during VSV infection
- Oligomycin disturbs mitochondrial structure-metabolism and limits viral replication
- MIC60 KO in CD11c<sup>+</sup> cells limits viral replication and prolonged immune activation
- Oligomycin and MIC60 deletion induce accumulation of anti-viral itaconate in BMDCs

Article

# Controlling mitochondrial membrane architecture via MIC60 determines viral replication to promote anti-viral immunity

Ichiro Katahira,<sup>1</sup> Nina Liebrand,<sup>1</sup> Michal Gorzkiewicz,<sup>1</sup> Niklas Paul Klahm,<sup>2</sup> Džuljeta Abromavičiūtė,<sup>1</sup> Julia Werner,<sup>1</sup> Karina Stephanie Krings,<sup>1</sup> Sarah Orywol,<sup>1</sup> Tobias Lautwein,<sup>3</sup> Karl Köhrer,<sup>3</sup> Diran Herebian,<sup>4</sup> Ertan Mayatepek,<sup>4</sup> Max Anstötz,<sup>5</sup> Ann Kathrin Bergmann,<sup>6</sup> Arun Kumar Kondadi,<sup>2</sup> Haifeng C. Xu,<sup>1</sup> Aleksandra A. Pandya,<sup>7,8,9</sup> Takumi Kobayashi,<sup>10,11</sup> Dirk Brenner,<sup>10,11,12</sup> Thomas Floss,<sup>13</sup> Ulrich Kalinke,<sup>14</sup> Andreas S. Reichert,<sup>2,15</sup> and Philipp A. Lang<sup>1,15,16,\*</sup>

<sup>1</sup>Department of Molecular Medicine II, Medical Faculty and University Hospital Düsseldorf, Heinrich Heine University Düsseldorf, Universitätsstrasse 1, Düsseldorf 40225, Germany

<sup>2</sup>Institute of Biochemistry and Molecular Biology I, Medical Faculty and University Hospital Düsseldorf, Heinrich Heine University Düsseldorf, Universitätsstrasse 1, Düsseldorf 40225, Germany

<sup>3</sup>Biological and Medical Research Center (BMFZ), Heinrich-Heine-University Düsseldorf, Universitätsstrasse 1, Düsseldorf D-40225, Germany

<sup>4</sup>Department of General Pediatrics, Neonatology and Pediatric Cardiology, Medical Faculty and University Hospital Düsseldorf, Heinrich-Heine-University, Düsseldorf, Germany

<sup>5</sup>Institute of Anatomy II, Medical Faculty and University Hospital, Heinrich Heine University Düsseldorf, Universitätsstrasse 1, 40225 Düsseldorf, Germany

<sup>6</sup>Core Facility for Electron Microscopy, Faculty of Medicine, Heinrich Heine University Düsseldorf, Düsseldorf, Germany

<sup>7</sup>Institute of Clinical Chemistry and Clinical Pharmacology, University Hospital Bonn, Venusberg-Campus 1, Bonn 53127, Germany

<sup>8</sup>German Center for Infection Research (DZIF), Partner Site Bonn-Cologne, Bonn, Germany

<sup>9</sup>University Hospital Düsseldorf, Department of Oncology, Hematology and Clinical Immunology, Moorenstrasse 5, Düsseldorf 40225, Germany

<sup>10</sup>Experimental and Molecular Immunology, Department of Infection and Immunity, Luxembourg Institute of Health, Esch-sur-Alzette, Luxembourg

<sup>11</sup>Immunology & Genetics, Luxembourg Centre for Systems Biomedicine (LCSB), University of Luxembourg, 7, Avenue des Hauts Fourneaux, Esch-sur-Alzette, Luxembourg

<sup>12</sup>Odense Research Center for Anaphylaxis (ORCA), Department of Dermatology and Allergy Center, Odense University Hospital, University of Southern Denmark, Odense, Denmark

<sup>13</sup>Helmholtz Zentrum München, Deutsches Forschungszentrum für Gesundheit und Umwelt, Neuherberg, Germany

<sup>14</sup>Institute for Experimental Infection Research, TWINCORE, Centre for Experimental and Clinical Infection Research, a joint venture between the Helmholtz Centre for Infection Research and the Hannover Medical School, Hannover, Germany

<sup>15</sup>These authors contributed equally

<sup>16</sup>Lead contact

\*Correspondence: [langp@uni-duesseldorf.de](mailto:langp@uni-duesseldorf.de)

<https://doi.org/10.1016/j.celrep.2025.115922>

## SUMMARY

Virus-infected cells often exhibit dramatic cellular changes accompanied by altered mitochondrial function. The contribution of factors shaping the inner mitochondrial membrane (IMM) and cristae architecture to viral replication is insufficiently understood. Single-cell transcriptomics applying vesicular stomatitis virus infection suggests involvement of factors determining IMM architecture following infection. Consistently, inhibition of the  $F_1F_0$  adenosine triphosphate (ATP) synthase reduces viral replication, which is associated with oligomerization of this complex and altered IMM structure. Moreover, deletion of mitochondrial contact site and cristae organizing system (MICOS) complex by targeting MIC60 results in reduced viral replication. Generation of *Mic60<sup>inv/inv</sup> CD11c-Cre<sup>+</sup>* mice uncovers reduced crista junctions and viral replication in bone marrow-derived dendritic cells. Consequently, reduced viral replication in CD11c-expressing cells limits prolonged immune activation. Altogether, by linking the  $F_1F_0$  ATP synthase and the MICOS complex to viral replication and immune activation, we describe links between the mitochondrial structure-metabolism and the immune response against viral infection.

## INTRODUCTION

Viral infections remain a global health problem with countless infections worldwide and potential risks for outbreaks causing enormous harm to humans and society. Viruses hijack the host cells to propagate and are therefore known to influence cellular processes. Mitochondria are essential organelles present in nearly all eukaryotic cells, having numerous metabolic and regulatory functions. Mitochondria provide energy for cellular processes by generating adenosine triphosphate (ATP) via oxidative phosphorylation (OXPHOS). This depends on the concerted action of the electron transport chain (ETC), with complexes I–IV, and the  $F_1F_0$  ATP synthase (complex V). Linked to their bioenergetic and metabolic functions, mitochondria also affect several key cellular programs, including innate immune activation and programmed cell death. The central role of mitochondria and related metabolic adaptation in orchestrating a diverse set of host-defense pathways has been recognized in recent years.<sup>1,2</sup>

Cellular energy metabolism depends on the proper organization of the inner mitochondrial membrane (IMM).<sup>3,4</sup> The IMM is subcompartmentalized into the inner boundary membrane (IBM), which opposes the outer membrane (OM), and the cristae membrane (CM), which represents invaginations of the IMM. The IBM and the CM are linked by pore- or slit-like structures with diameters ranging from 12 to 40 nm, termed crista junctions (CJs).<sup>4,5</sup> Several proteins are known to affect cristae morphology, yet three important players are directly involved: the mitochondrial contact site and cristae organizing system (MICOS) complex, the dynamin-like GTPase OPA1, and the  $F_1F_0$  ATP synthase.<sup>5–9</sup> MIC60 is an essential member of the MICOS complex and the core subunit required for CJ formation, as shown for numerous organisms.<sup>3,9,10</sup> MIC60 has been further shown to physically interact with OPA1,<sup>9,11</sup> and in baker's yeast the MICOS complex functionally and physically interacts with the  $F_1F_0$  ATP synthase.<sup>12,13</sup> Notably, cristae are highly dynamic and are remodeled at a timescale of seconds in a MICOS-dependent manner.<sup>13–15</sup> It has been proposed that this remodeling has important implications for bioenergetic and metabolic properties, in particular with respect to metabolic adaptations.

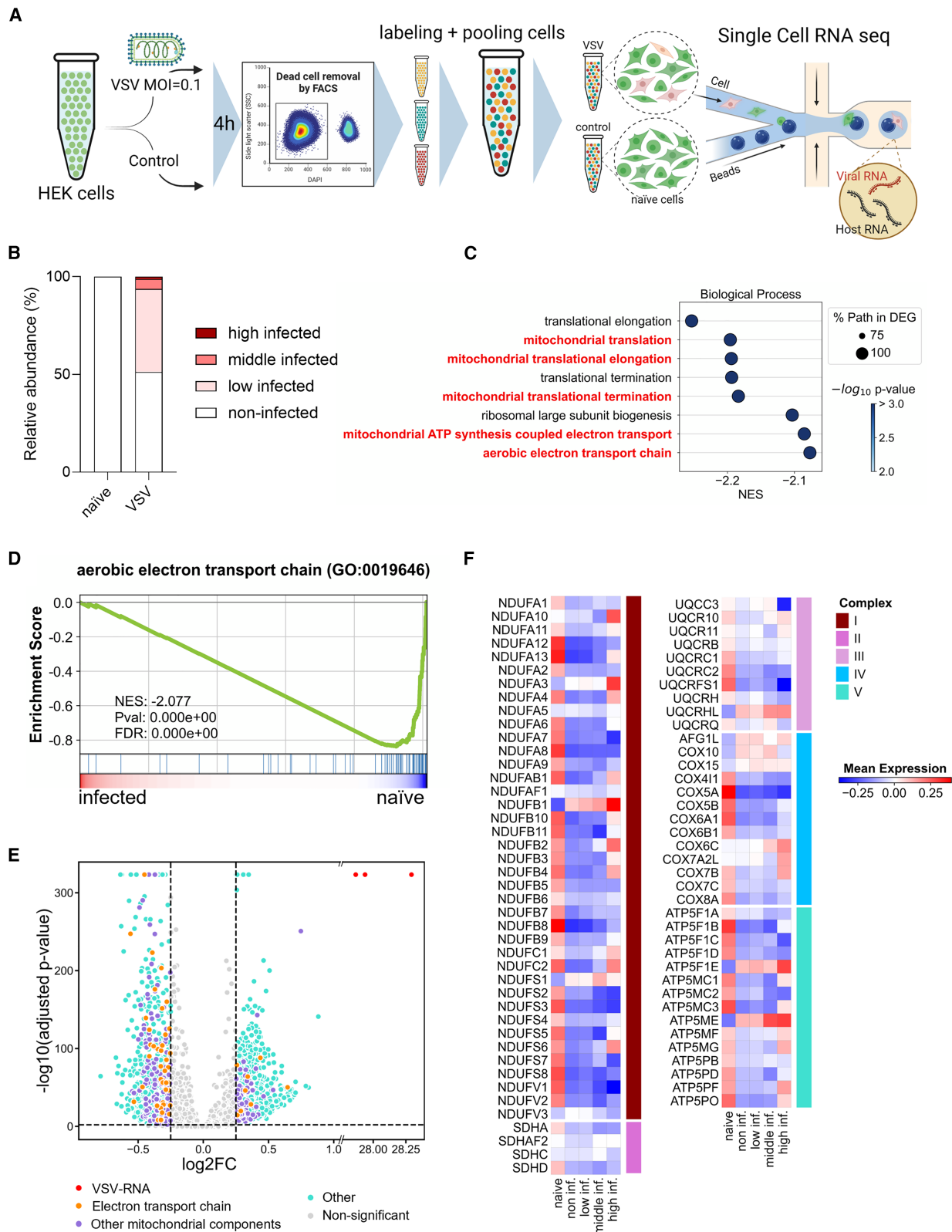
Mitochondrial structure and metabolism are closely linked in a dynamic equilibrium, with each influencing the other to maintain cellular homeostasis. How cristae structure and the MICOS complex affect metabolic flux is not clear; however, CJs were proposed to determine the distribution of membrane complexes within the inner membrane. Moreover, mitochondrial fusion and fission processes directly impact metabolic efficiency. Fusion allows for the mixing of mitochondrial contents, optimizing energy production and metabolic capacity.<sup>16</sup> Conversely, fission facilitates the segregation of damaged mitochondria, maintaining overall metabolic health.<sup>17</sup> On the other hand, metabolic regulation of mitochondrial membrane structure is also not negligible. Changes in metabolic demands can alter cristae organization, directly affecting ATP production efficiency.<sup>18</sup> Decreased mitochondrial membrane potential (MMP) can promote cleavage of OPA1, resulting in accumulation of short form OPA1 (S-OPA1), which can induce mitochondrial fission. In addition, MIC60 is responsible for IMM-OM tethering, which can be detached by S-OPA1, thus changing the IMM structure.<sup>19</sup> In line with this,

disturbed MMP by uncoupling compounds, such as nigericin and FCCP, results in disrupted cristae structures, including loss of lamellar cristae organization and reduced CJs.<sup>20</sup> This bidirectional relationship ensures that mitochondrial structure adapts to meet cellular metabolic needs while maintaining organelle health and function. It is evident that this relationship is complex and multi-level, involving a significant number of aspects.

After viral infection, host cells can switch to aerobic glycolysis, termed the Warburg effect, which can be also observed in cancer cells and rapidly proliferating lymphocytes.<sup>21,22</sup> Accompanied by this metabolic shift, the disturbance of tricarboxylic acid (TCA) cycle can result in the accumulation of specific antimicrobial metabolites that are recently recognized as a constitutive innate immune response.<sup>23</sup> These include lactate,<sup>23</sup> itaconate, and fumarate.<sup>24</sup> Itaconate is a metabolite generated from *cis*-aconitate as a bypath of the TCA cycle, with the ability to directly inhibit mitochondrial succinate dehydrogenase. Interestingly, various infections and immune activation can result in the accumulation of itaconate,<sup>22,25,26</sup> which exhibits anti-inflammatory capacities<sup>27</sup> and anti-viral functions in macrophages and neurons.<sup>22,28</sup> However, the detailed mechanisms of how these metabolites restrict viral infections are still unclear.

Mitochondria and, in particular, factors that determine cristae morphology have recently been recognized to play critical roles in innate immune activation. Mitochondria can release damage-associated molecular patterns, which activate innate immunity. Specifically, mitochondrial DNA (mtDNA) and double-stranded RNA are both able to activate cytosolic pattern recognition receptors (PRRs) to induce cytokine production.<sup>29,30</sup> Cristae organization can affect mtDNA and mitochondrial RNA (mtRNA) release and consequently innate immune activation,<sup>31</sup> and disturbed enzymatic activity in the TCA cycle can promote formation of mitochondria-derived vesicles hosting mtDNA to activate cGAS/STING.<sup>24,32</sup> Recently, it has been reported that itaconate induces type I interferon (IFN) production by promoting mtRNA release at early stages of infection.<sup>33</sup> While these mechanisms promote anti-viral immunity and accordingly limit viral replication, the role of the MICOS complex regarding immune activation and infection has been insufficiently studied.

To identify factors driving viral infection and propagation we analyzed transcripts of partly infected cells at a single cell level using the vesicular stomatitis virus (VSV) model system. We found mitochondrial gene expression clusters significantly downregulated in infected cells, and further analysis suggested an important role of factors regulating IMM architecture. Pharmacological inhibition of ETC complex showed an anti-viral effect, with the most potent effect being observed for inhibition of  $F_1F_0$  ATP synthase. Accordingly, inhibition of  $F_1F_0$  ATP synthase altered the cristae structure accompanied by increased oligomers/dimers of ATP synthase. As a model of disrupted IMM architecture, we generated mice deficient for the MICOS-essential protein MIC60. We found reduced viral replication in MIC60-deficient bone marrow derived dendritic cells (BMDCs), associated with the intracellular accumulation of itaconate. In mice, reduced viral replication in MIC60-deficient CD11c<sup>+</sup> cells was accompanied with reduced prolonged immune activation after infection. Taken together, we discovered links between



(legend on next page)



the IMM organization and viral infection and corresponding immunity.

## RESULTS

### Mitochondria gene expression clusters are impoverished in VSV-infected cells

To uncover host cell factors driving viral infection and propagation, we infected human embryonic kidney (HEK) cells with VSV. To obtain both non-infected and infected cells from VSV-exposed cells, we used a multiplicity of infection (MOI) of less than 1 (Figures 1A and S1A). To investigate an early time point, the frequency of infected cells was quantified after adding monensin at 4 h after infection followed by measurement of VSV-G on the surface 24 h later (Figure S1A). Notably, while the cells were infected at an MOI of 0.1, a higher frequency of the cells were identified to be VSV-G positive after 24 h, indicating that a proportion of cells have already been reinfected at 4 h after VSV exposure. In addition, we included naive cells, which have not been exposed to virus as a control (Figures 1A and S1A). We sorted cell suspensions for viability (Figure S1B), barcoded three naive and three VSV-infected cell suspensions followed by pooled single-cell transcriptomic analysis (Figure 1A). We analyzed 19,227 cells, with 7,358 being from naive samples and 11,869 VSV-exposed cells. As expected, we found VSV transcripts only in approximately 50% of the cells which have been exposed to VSV, in sharp contrast to naive cells (Figure 1B). Notably, we identified cells with high, medium, and low VSV transcript levels, which potentially refer to replication cycle subsets reflecting the temporal increase in VSV RNA levels throughout infection (Figures 1B and S1C). When we compared VSV-infected cells with naive samples, several gene ontology clusters affecting mitochondrial energy metabolism and translation were enriched in non-infected cells when compared with infected cells (Figure 1C). Interestingly, mitochondrial ATP synthesis-coupled electron transport and aerobic ETC were among the significant clusters identified in naive cells when compared with infected cells (Figures 1C and 1D). Combined, several genes encoding for mitochondrial components or OXPHOS were differentially regulated in infected cells when compared with naive cells (Figures 1E and 1F). Notably, most of those genes required for OXPHOS were downregulated in single-cell RNA sequencing (scRNA-seq) analysis in infected cells, when compared with naive cells (Figures 1E and 1F). Next, we wondered whether viral infection will generally result in the down-regulation of genes encoding for proteins of the ETC. However, we observed only significantly reduced UQCRC1 mRNA levels when we infected

cells with a high MOI of VSV and herpes simplex virus (HSV) followed by analysis of isolated RNA from all cells, while other viral infections did not affect this gene expression (Figures S1D–S1H). These data suggest that VSV infection can be associated with the down-regulation of genes affecting OXPHOS, while the causality and its significance remain unclear.

Accordingly, we used pharmacological inhibitors affecting OXPHOS complexes to investigate their impact on viral replication. While rotenone and antimycin A (AA) inhibit complex I and complex III of the ETC, respectively, oligomycin inhibits the mitochondrial  $F_1F_0$  ATP synthase.<sup>34</sup> As expected, we measured a marked reduction of the oxygen consumption rate after oligomycin or rotenone/AA treatment of cells, which indicates that these inhibitors effectively blocked OXPHOS in this setting (Figures 2A and 2B). Notably, cell death was not induced by oligomycin in this setting, while rotenone/AA induced moderate formation of early apoptotic cells (Figure S2A). Since the tissue culture medium contains glucose, ATP levels in cell lysates were also similar in control, oligomycin-treated or rotenone/AA-treated cells (Figure S2B). However, when we determined VSV plaque formation in the presence of oligomycin, we found an inhibition of VSV plaque formation (Figure S2C). Interestingly, we did not observe this inhibitory effect with treatment of rotenone/AA in this setting (Figure S2C). Furthermore, when we infected cells during oligomycin or rotenone/AA treatment, we found strongly reduced VSV transcript levels in oligomycin-treated cells (Figure 2C). Notably, VSV transcript levels were also reduced during treatment with rotenone/AA, but remained at significantly higher levels than observed in samples from oligomycin-treated cells (Figure 2C). Moreover, VSV titers in the supernatant of infected cells were highly reduced after treatment with oligomycin, while we observed only a modest but significant difference in rotenone/AA-treated cells (Figure 2D). These data indicate that the inhibition of OXPHOS can result in reduced viral replication after VSV infection. However, inhibition of the  $F_1F_0$  ATP synthase resulted in a robust blockade of viral replication, while inhibition of complexes I and III resulted in only moderate effects.

To determine if the observed phenomenon is specific for VSV infection, we analyzed replication of other viruses in the presence of oligomycin, rotenone or AA. We observed reduced Zika virus (ZIKV, both the American and the African strains) titer after oligomycin treatment, while there was no significant change after rotenone or AA treatment in this setting (Figures 2E and 2F). Similar effect was observed in case of severe acute respiratory syndrome coronavirus 2 (SARS-CoV-2) (B.1.1.7 strain) infection, where an inhibition of the CPE score was observed after oligomycin treatment (Figures S2D–S2F). An inhibitory effect of

### Figure 1. scRNA-seq reveals altered mitochondria gene expression after VSV infection

- (A) Schematic of procedures for scRNA-seq; illustration was generated with Biorender.com.  
 (B) VSV-infected cells were classified according to relative abundance of VSV transcript to total RNA: high-infected cells (>0.1% of VSV transcripts), middle-infected cells (0.01%–0.1%), and low-infected cells ( $\leq 0.01\%$ , >0%).  
 (C) Normalized enrichment score (NES) in gene set enrichment analysis (GSEA) for the biological process (Gene Ontology [GO]: 0008150) of VSV-infected cells to naive cells. Dot sizes indicate the number of genes in the respective gene set that overlap with the differentially expressed genes (DEGs). Gene sets shown in red are associated with mitochondria.  
 (D) GSEA showing genes associated with the aerobic ETC (GO: 0019646) are enriched in naive cells compared with infected cells. NES and false discovery rate (FDR) are shown.  
 (E) Volcano plots showing the log2 fold-change and adjusted *p* values in gene expression values of VSV-infected cells relative to naive cells.  
 (F) Heatmap showing mean expression of genes associated with the component of ETC in each infectious status.

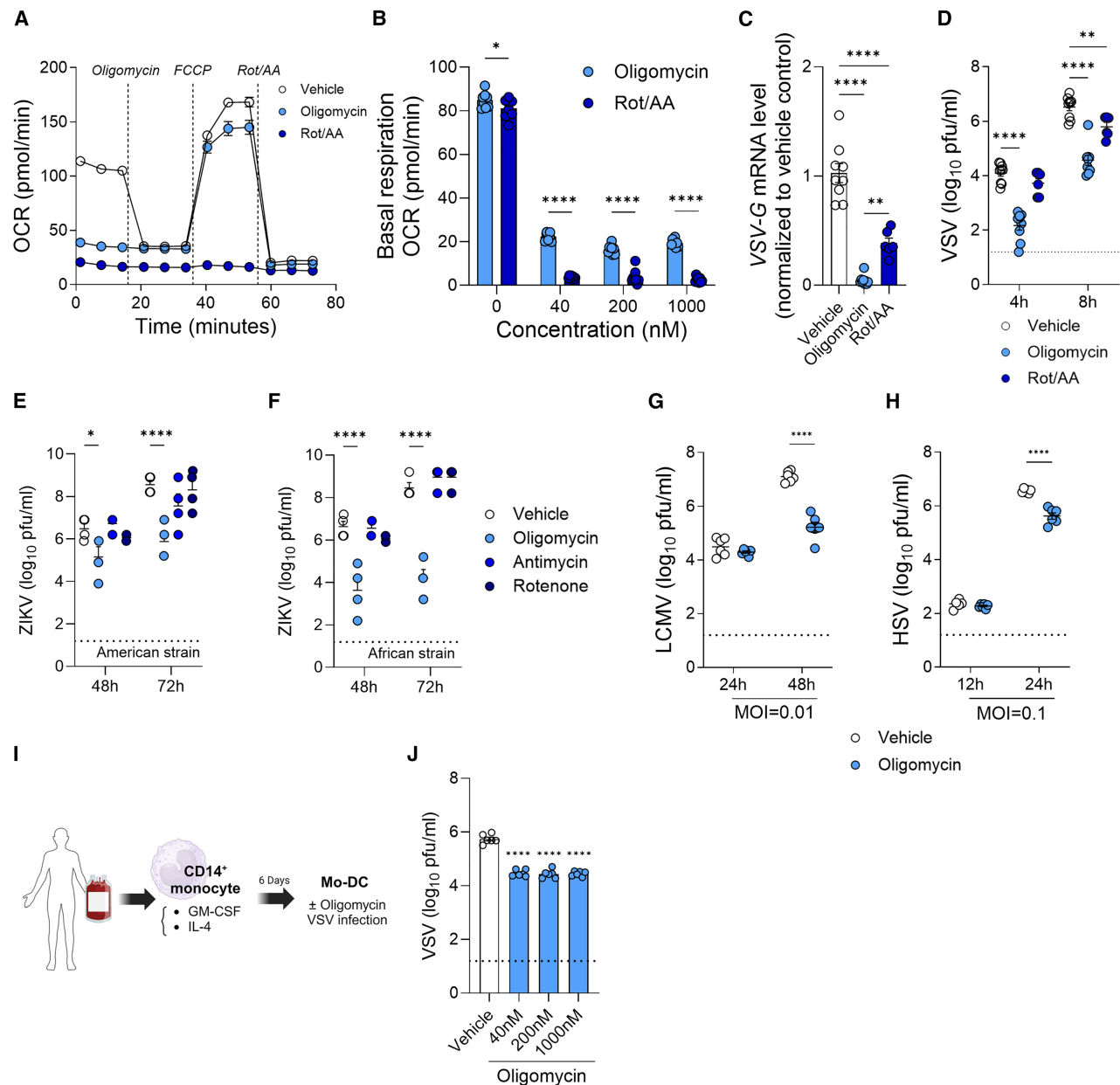


**Figure 2. Inhibition of OXPHOS complexes reduces viral replication**

(A and B) (A) Oxygen consumption rate (OCR) was measured in Vero cells pre-treated with 200 nM of oligomycin, rotenone/AA (Rot/AA) or DMSO (vehicle). (B) Basal respiration after treatment with the indicated concentration of oligomycin or Rot/AA; data from two experiments are shown. Significance was determined by ordinary two-way ANOVA followed by Sidak's multiple comparisons test.  $p < 0.05$ ,  $****p < 0.0001$ . Data are presented as mean  $\pm$  SEM. (C and D) Vero cells were infected with VSV at an MOI of 0.01 after the pre-treatment with 200 nM of oligomycin, 500 nM of Rot/AA or vehicle for 20 min (C) mRNA expression of VSV glycoprotein (VSV-G) at 8 h post infection, (D) VSV titer in the supernatant; data were from three experiments for oligomycin and vehicle control and two experiments for Rot/AA.  $p$  values were determined using ordinary one-way ANOVA with Tukey's multiple comparisons test (C) and ordinary two-way ANOVA followed by Sidak's multiple comparisons test (D).  $**p < 0.01$ ,  $****p < 0.0001$ . Data are presented as mean  $\pm$  SEM. (E and F) Vero cells were infected with (E) ZIKV (American strain) and (F) ZIKV (African strain) at an MOI of 0.001 after pre-treatment with 10  $\mu$ M oligomycin, antimycin, rotenone or vehicle control for 20 min. Virus titer in the supernatant was measured at the indicated time points; data from four experiments are shown. Significance was determined by ordinary two-way ANOVA with Dunnett's multiple comparisons test.  $*p < 0.05$ ,  $****p < 0.0001$ . Data are represented as mean  $\pm$  SEM. (G and H) Vero cells were treated with 200 nM oligomycin or vehicle control followed by infection with (G) LCMV-WE at an MOI of 0.01 or (H) HSV-F1 at an MOI of 0.1. Virus titer in collected supernatants was measured at the indicated time points; data from two experiments are shown. Statistical significance was determined by ordinary two-way ANOVA followed by Sidak's multiple comparisons test.  $****p < 0.0001$ . Data are represented as mean  $\pm$  SEM.

(legend continued on next page)

oligomycin was also observed for lymphocytic choriomeningitis virus (LCMV WE strain) and HSV (HSV-F1 strain) (Figures 2G and 2H), and further for VSV in human primary cells, when monocyte-derived dendritic cells were generated from CD14<sup>+</sup> monocytes out of buffy coats (Figures 2I and 2J). Taken together, these data show that viral replication can be inhibited by oligomycin following infection with VSV, SARS-CoV2, ZIKV, LCMV, and HSV in tissue culture settings.

### Mitochondrial structure-metabolism affects viral replication

The observation that anti-viral effects of OXPHOS inhibition differed depending on the targeted OXPHOS complexes prompted us to investigate further which factors drive anti-viral effects. We analyzed 12 clusters identified by their gene expression profile in single cell transcriptomics following naive and infected cells (Figures 1A and 3A). Interestingly, one cluster (cluster 11) with highly infected cells was identified, while one cluster (cluster 9) showed a relatively large proportion of naive cells (Figures 3B and S3A). To depict the patterns that may critically influence infection and VSV replication, these two clusters were compared. Between both clusters, 1,497 significantly different RNA expression levels were detected. Gene ontology cluster analysis highlighted that the ‘mitochondrial inner membrane’ cluster was down-regulated in VSV-infected cells (cluster 11) when compared with cells from cluster 9 (Figures 3C–3E). The genes differentially expressed between the two clusters included subunits of the F<sub>1</sub>F<sub>0</sub> ATP synthase and the MICOS complex as well as other proteins known to regulate IMM architecture (Figure 3F). Accordingly, we speculated that the organization of the IMM might be affected after viral infection. Notably, the F<sub>1</sub>F<sub>0</sub> ATP synthase does not solely contribute to ATP production, but also has a structural, non-enzymatic role in shaping the IMM as dimers and oligomers of this complex determining cristae morphology by imposing a positive membrane curvature.<sup>8,35,36</sup> To address whether oligomycin alters oligomer formation of the F<sub>1</sub>F<sub>0</sub> ATP synthase, we used BN-PAGE analysis. Indeed, we observed that 4- and 8-h oligomycin treatment triggers formation of oligomers/dimers of the F<sub>1</sub>F<sub>0</sub> ATP synthase in contrast to rotenone/AA treatment in this setting (Figure 3G). Using transmission electron microscopy, we found that the number of mitochondria was increased and the mitochondrial area was reduced consistent with overall mitochondrial fragmentation (Figures 3H–3J). Importantly, we also found that oligomycin treatment led to decreased numbers of CJs and increased cristae width (Figures 3K and 3L) demonstrating that oligomycin indeed affects cristae morphology and CJ formation. Notably, tighter cristae with reduced width were proposed to be more efficient in OXPHOS due to the clustering of proteins and metabolites important for metabolic functions in close proximity.<sup>6,37</sup> Compared with oligomycin, we observed only modest alterations of IMM architecture after rotenone/AA treatment in this setting (Figures S3B–S3D). Notably, oligomycin and rotenone or AA have an opposite effect on MMP, since complexes I and III build

up a proton gradient, while the F<sub>1</sub>F<sub>0</sub> ATP synthases consume it for ATP production. Some ionophores or uncouplers such as nigericin, salinomycin, nanchangmycin, narasin, maduramycin, and CCCP/FCCP, are known to disrupt the MMP and also to disturb cristae morphology.<sup>20,38</sup> Also, those compounds showed potent inhibitory effects on VSV replication (Figures S3E) without significantly affecting cell viability in this setting (Figures S3F). Accordingly, we speculate that disrupted cristae organization and the consequent altered metabolic functions are responsible for the observed anti-viral effects in oligomycin-treated cells.

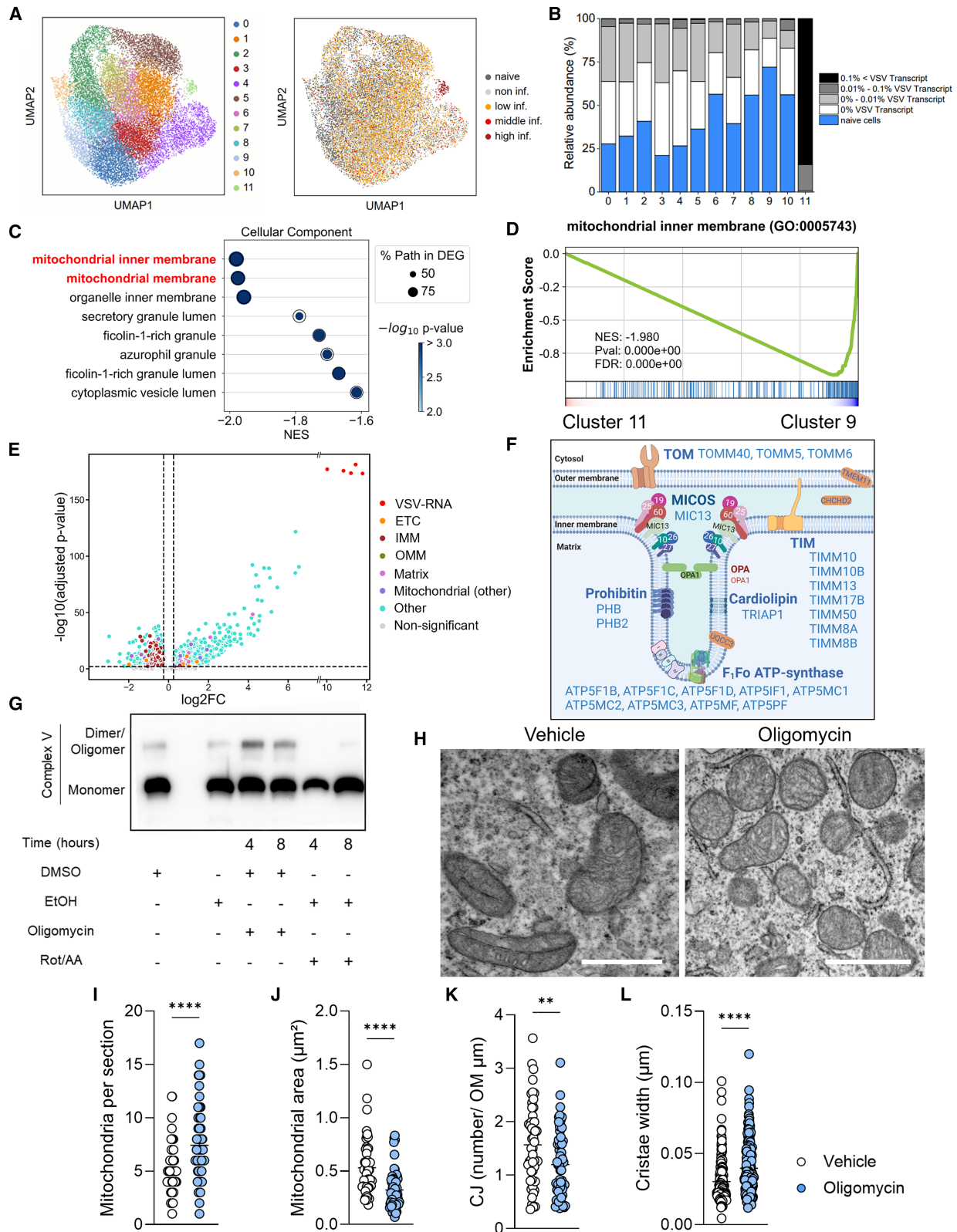
### Disrupted cristae structure by MIC60 deficiency is linked to reduced viral replication

To further investigate the role of IMM organization, we used cells deficient for the central component of the MICOS complex MIC60/IMMT/mitofilin as a model of disrupted cristae formation.<sup>10,36</sup> As expected, we found alterations in inner membrane morphology, which was associated with reduced abundance of CJs and an increased width of cristae in the absence of MIC60, when compared with MIC60-competent cells (Figures 4A–4D). Interestingly, after infection of HAP1 cells, cristae width was observed to increase further in MIC60-competent as well as in MIC60-deficient cells (Figure 4D). Accordingly, focused ion beam scanning electron microscopy analysis was performed with VSV-infected cells and showed fragmented and rather spherical mitochondria in MIC60-deficient cells while MIC60-competent cells maintain largely tubular and extended mitochondria (Figures 4E and 4F). When VSV transcripts were analyzed in MIC60-competent and -deficient cells, reduced VSV RNA expression levels could be detected in the absence of MIC60 (Figure 4G). Consistently, when we measured the presence of infectious viral particles in the supernatant of infected cells, reduced VSV as well as LCMV titers could be determined in MIC60-deficient cells when compared with MIC60-competent cells (Figures 4H and S4A). Taken together, these data indicate that the deletion of MIC60 not only results in altered cristae architecture and loss of CJs but also in reduced viral replication.

### MIC60 drives viral replication and innate immune activation in antigen-presenting cells

Next, we wondered whether MIC60 may likewise affect viral replication in antigen-presenting cells and consequently innate immune activation. Hence, we generated *Mic60<sup>inv/inv</sup>* × *CD11c-Cre<sup>+</sup>* mice, where MIC60 was conditionally deleted in CD11c-expressing cells (Figures S5A and S5B). As expected, the deletion of MIC60 resulted in significantly decreased CJs in BMDCs (Figures S5C and S5D). To investigate VSV replication in antigen-presenting cells, BMDCs were generated from *Mic60<sup>inv/inv</sup>* × *CD11c-Cre<sup>+</sup>* and control mice followed by infection with VSV (Figure 5A).<sup>39,40</sup> In line with the results from HAP1 cells described above, we found reduced expression of VSV transcripts in MIC60-deficient BMDCs when compared with wild-type (WT) cells (Figure 5B). Consistently, the VSV titer in the supernatant of

(I and J) Human monocyte-derived dendritic cells (Mo-DCs) were differentiated from PBMCs and treated with oligomycin for 20 min followed by infection with VSV at an MOI of 0.1. (J) Viral titer was measured 8 h post infection; illustration was created with [Biorender.com](https://www.biorender.com); data from two biological donors are shown. *p* values were determined by ordinary one-way ANOVA with Tukey’s multiple comparisons test. \*\*\*\**p* < 0.0001. Data are represented as mean ± SEM.



(legend on next page)



BMDCs was reduced when MIC60 was absent (Figure 5C). Notably, we also observed reduced LCMV titers in the supernatant of MIC60-deficient BMDCs (Figure S5E). When we analyzed mRNA levels of genes encoding for innate immune activation at later time points after infection, we found significantly reduced *Cxcl10* expression in the absence of MIC60, which is likely due to reduced viral replication (Figure 5D). Consistently, IFN- $\alpha$  protein levels in the supernatant of BMDCs were significantly reduced in MIC60-deficient BMDCs at later time points (Figure 5E). We also observed reduced production of other pro-inflammatory factors in MIC60-deficient DCs (Figure 5F). Notably, when we measured co-stimulatory molecules, we found reduced expression of CD86, CD40 and MHC-II in *Mic60*<sup>-/-</sup> DCs when compared with WT DCs (Figures 5G–5I and S5F). These data suggested that the deletion of MIC60 results in reduced viral replication in BMDCs. As a consequence, reduced viral replication caused lower innate immune activation in MIC60-deficient antigen-presenting cells after infection.

### Absence of MIC60 results in disturbance of the TCA cycle and accumulation of anti-viral itaconate

Next, we wondered by which mechanism MIC60-deficient BMDCs exhibited reduced viral replication. Since cell death can affect viral replication and VSV is a cytolytic virus, we wondered whether MIC60 affected cell viability during infection. However, we did not observe a difference in early or late apoptotic cells in this setting (Figure S5G). Moreover, we speculated that MIC60 deficiency might affect vesicular transport and accordingly viral uptake into cells. However, viral entry was not impaired in MIC60-deficient BMDCs when compared with WT controls (Figures S5H). Since mitochondrial reactive oxygen species (ROS) can interfere with viral replication, we speculated that an altered IMM organization in DCs might result in aberrant ROS production or MMP. However, Mitosox as well as TMRM staining in BMDCs were similar in the absence and presence of MIC60 after infection (Figures S5I and S5J).

Next, we conducted Seahorse analysis to investigate the impact of MIC60 on mitochondrial metabolic functions. Basal mitochon-

drial respiration was similar in MIC60-competent and MIC60-deficient BMDCs without infection and significantly decreased in both groups following infection with VSV (Figure 6A). Notably, MIC60-deficient cells retained higher basal respiration compared with control cells after infection (Figure 6A). Furthermore, we found reduced maximal respiration in MIC60-deficient BMDCs when compared with controls in the absence of infection (Figure 6B). Basal glycolysis was increased in the absence of MIC60, indicating a greater proportion of glycolysis on cellular metabolic functions than in control cells (Figures 6C and 6D). However, after infection, the proportion of glycolysis increased in both WT and MIC60-deficient BMDCs (Figure 6D). Taken together, these data indicate that MIC60 deficiency affected mitochondrial metabolism and resulted in increased basal glycolysis, but the observed effects were rather modest.

Next, we performed a targeted analysis of metabolites of infected BMDCs. We observed increased concentrations of several metabolites generated during glycolysis after infection with VSV, indicating a metabolic shift toward aerobic glycolysis (Figure 6E). Interestingly, this effect was not dependent on MIC60, since also in MIC60-deficient BMDCs, increased metabolites relating to aerobic glycolysis were observed (Figure 6E). Furthermore, we identified strongly decreased levels of acetyl-CoA after infection with VSV in both groups (Figure 6E). Consistently, ATP concentrations were highly reduced, accompanied by increased AMP levels after infection with VSV in both groups (Figure 6E). However, oxaloacetic acid was significantly increased in naive MIC60-deficient cells when compared with naive MIC60-competent cells (Figures 6E and S6A). Oxaloacetic acid is part of the TCA cycle producing citrate after condensation with acetyl-co-enzyme A. Furthermore, this metabolite affects the reactions using  $\alpha$ -ketoglutarate (KG), aspartate, and glutamine.<sup>41–43</sup> Hence, we speculated that the processes following glucose and glutamine metabolism might be affected by MIC60. To depict changes in metabolic glucose and glutamine cascades, we performed tracer experiments using <sup>13</sup>C-labelled glucose and <sup>13</sup>C-labelled glutamine followed by mass spectrometry analyses (Figure S6B). Notably, we selected an early time point to investigate the consumption of metabolites during the short infection time we used earlier. Specifically, we

### Figure 3. Unbiased cluster analysis suggests the importance of the IMM during VSV infection

- (A) UMAP representation showing the twelve clusters (left) and distribution of the naive, non-, low-, middle-, and high-infected cells between the clusters (right).  
 (B) Relative abundance of the naive, non-, low-, middle-, and high-infected cells in each cluster.  
 (C) Normalized enrichment score (NES) in gene set enrichment analysis (GSEA) for the cellular component (Gene Ontology [GO]: 0005575) of cluster 11 ("infected cluster") compared with cluster 9 ("non-infected cluster"). Dot sizes indicate the number of genes in the respective gene set that overlap with the differentially expressed genes (DEGs).  
 (D) GSEA showing genes associated with the mitochondrial inner membrane are enriched in cluster 9 ("non-infected cluster") compared with cluster 11 ("infected cluster"). NES and false discovery rate (FDR) are shown.  
 (E) Volcano plots showing the log<sub>2</sub> fold-change and adjusted *p* values in gene expression values in cluster 11 ("infected cluster") relative to cluster 9 ("non-infected cluster").  
 (F) Schematic of the components organizing mitochondrial membrane. The genes showing in red were up-regulated and blue were down-regulated in the cluster 11 ("infected cluster") compared with cluster 9 ("non-infected cluster"); illustration was made with [Biorender.com](https://biorender.com).  
 (G) HEK cells were treated with 200 nM oligomycin, 500 nM Rot/AA, or vehicles for the indicated time. The oligomeric state of the F<sub>1</sub>F<sub>0</sub> ATP synthase was analyzed in digitonin solubilized isolated mitochondria by BN-PAGE; image is representative of three independent experiments for oligomycin and two experiments for Rot/AA.  
 (H) Representative transmission electron microscopy (TEM) micrographs of Vero cells treated with 200 nM oligomycin or vehicle; scale bar, 1  $\mu$ m; data are representative of two independent experiments.  
 (I–L) Quantification of TEM micrographs of Vero cells treated with 200 nM oligomycin or vehicle. (I) Number of mitochondria per section, (J) mitochondrial area, (K) number of CJs, and (L) cristae width; data were from two independent experiments. *p* values were determined using two-tailed/unpaired Student's *t* test. \*\**p* < 0.01, \*\*\*\**p* < 0.0001.

Data are represented as mean  $\pm$  SEM.





preincubated the samples for 2 h with the labeled glucose or glutamine followed by infection with VSV and collected the samples 4 h after infection (Figure S6C). Interestingly, when we monitored the incorporation of  $^{13}\text{C}$  into the metabolites, we observed only modest changes throughout the metabolites tested (Figures S6D–S6H). However, when we measured the levels of itaconate, a metabolite associated with inhibition of viral replication,<sup>28</sup> we observed increased concentrations in samples harvested from MIC60-deficient BMDCs when compared with controls (Figure 6F). Accordingly, we treated MIC60-competent BMDCs with itaconate for 3 or 12 h, followed by VSV infection. In itaconate-treated cells, significantly reduced VSV transcripts levels were observed (Figure 6G). Consistently, VSV titer was significantly decreased by itaconate in MIC60-competent BMDCs, but this inhibition was not observed in MIC60-deficient BMDCs (Figure 6H). Notably, itaconate was also rapidly accumulated in oligomycin-treated BMDCs, with subsequent reduction being observed during prolonged incubation times (Figure 6I).

Disruption of the IMM organization or disrupted TCA cycle results in the accumulation of specific metabolites such as itaconate or fumarate,<sup>24</sup> which in turn promote the release of mitochondrial nucleotides into cytosol, leading to increased innate immune activation.<sup>29,31</sup> Accordingly, we determined cytosolic mtDNA levels in BMDCs after VSV infection; however, we did not observe a significant difference between MIC60-competent and MIC60-deficient BMDCs in this setting (Figure S6I and S6J). Next, we measured cytosolic mtRNA levels in MIC60 HAP1 cells before or after VSV infection, and we found that mtRNA release is significantly increased in the absence of MIC60 in HAP1 cells after VSV infection (Figures 6J and 6K). This is consistent with a recent report suggesting that itaconate induces mtRNA-mediated type I IFN production.<sup>33</sup> Accordingly, early after VSV infection, increased mRNA expression levels of *Irfn1* and *Irfn4* were measured in MIC60-deficient BMDCs (Figure 6L and 6M). Notably, we also observed increased *Irfn1* and *Irfn4* mRNA levels in the absence of MIC60 after 4 h of treatment with the RIG-I agonist 3p-hpRNA (Figures 6N and 6O).

Overall, these data suggest that absence of MIC60 as well as the inhibition of another cristae shaping factor, the  $\text{F}_1\text{F}_0$  ATP synthase, affects mitochondrial metabolic functions, which is associated with increased concentrations of itaconate.

### MIC60 expression in CD11c-expressing cells promotes immune activation following viral infection

To further analyze the *in vivo* role of MIC60 in antigen-presenting cells, we infected *Mic60<sup>inv/inv</sup> × CD11c-Cre<sup>+</sup>* and WT mice intravenously with VSV. After infection, VSV initially replicates in CD169<sup>+</sup> CD11c<sup>Int</sup> cells that direct protective immunity through promoting cytokine production, antigen presentation, and activation of adaptive immunity.<sup>39,44</sup> Since CD169<sup>+</sup> cells can be modified via expression strategies utilizing the CD11c promoter,<sup>44</sup> we wondered whether the absence of MIC60 could reduce viral replication in

these cells and, consequently, immune activation. When snap frozen spleen tissue sections from *Mic60<sup>inv/inv</sup> × CD11c-Cre<sup>+</sup>* and WT mice were analyzed, we observed abundant VSV-infected CD169<sup>+</sup> cells in WT animals, but reduced in *Mic60<sup>inv/inv</sup> × CD11c-Cre<sup>+</sup>* mice (Figure 7A). Notably, CD169<sup>+</sup> cells were detected in both spleen tissue samples harvested from *Mic60<sup>inv/inv</sup> × CD11c-Cre<sup>+</sup>* and control mice, while VSV-G expression was reduced in spleen sections from *Mic60<sup>inv/inv</sup> × CD11c-Cre<sup>+</sup>* mice compared with controls (Figures 7A–7C). Consistently, when we infected mice with a lower dose, we observed VSV replication in spleen tissue of WT, but not *Mic60<sup>inv/inv</sup> × CD11c-Cre<sup>+</sup>* mice, which indicates that viral replication is impaired in the absence of MIC60 in CD11c-expressing cells (Figure 7D). As a consequence, innate type I IFN production was highly reduced in *Mic60<sup>inv/inv</sup> × CD11c-Cre<sup>+</sup>* mice when compared with WT controls (Figure 7E). This resulted in a reduced expression of IFN-stimulated genes after VSV infection in spleen tissue harvested from *Mic60<sup>inv/inv</sup> × CD11c-Cre<sup>+</sup>* mice compared with WT controls (Figures 7F–7H). Moreover, anti-VSV neutralizing IgG production was delayed in these animals (Figure 7I). Notably, the VSV infection remained controlled and mice did not show signs of pathology in this setting, likely because of reduced VSV replication after infection. Taken together, these data show that the deletion of MIC60 in CD11<sup>+</sup> cells resulted in limited viral replication after VSV infection of mice and consequently reduced immune activation.

## DISCUSSION

In the present study, we describe a link between the IMM architecture and mitochondrial metabolism during viral infection. In line with our findings that genes linked to ETC are affected upon VSV infection, inhibition of the  $\text{F}_1\text{F}_0$  ATP synthase had strong inhibitory effects on viral replication. Next to its role in ATP generation, this complex is well known to assemble into dimers and oligomers, which determine cristae architecture by imposing a positive membrane curvature, but these higher-order assembly states do not grossly affect the enzymatic activity.<sup>8,35,36</sup> Also, the addition of oligomycin did not grossly affect ATP levels, presumably by a compensatory switch to glycolysis. We observed that inhibiting the  $\text{F}_1\text{F}_0$  ATP synthase specifically triggers the formation of oligomers and dimers of the  $\text{F}_1\text{F}_0$  ATP synthase. Moreover, oligomycin altered the IMM structure; at the same time, we observed only modest alterations in IMM after rotenone/AA treatment in our settings. These data corroborate the view that the non-enzymatic property of the  $\text{F}_1\text{F}_0$  ATP synthase might contribute to the observed antiviral effects.  $\text{K}^+/\text{H}^+$  ionophores with uncoupling activity can modulate cristae structure and regulate apoptosis and inflammasome activation.<sup>20</sup> We observed a significant decrease of VSV replication after treatment with those ionophores, further supporting our hypothesis that mitochondrial inner membrane structure and the associated metabolic changes can affect viral infection. Indeed, oligomycin is well known to increase MMP by inhibiting ATP

(G and H) MIC60-deficient and competent HAP1 cells were infected with VSV at an MOI of 0.1. (G) VSV-G mRNA expression at 8 h post infection, (H) VSV titer in the infected supernatant; data are representative of two experiments. *p* values were determined using two-tailed/unpaired Student's *t* test (G) and ordinary two-way ANOVA followed by Sidak's multiple comparisons test (H). \*\**p* < 0.01, \*\*\*\**p* < 0.0001. Data are presented as mean ± SEM.

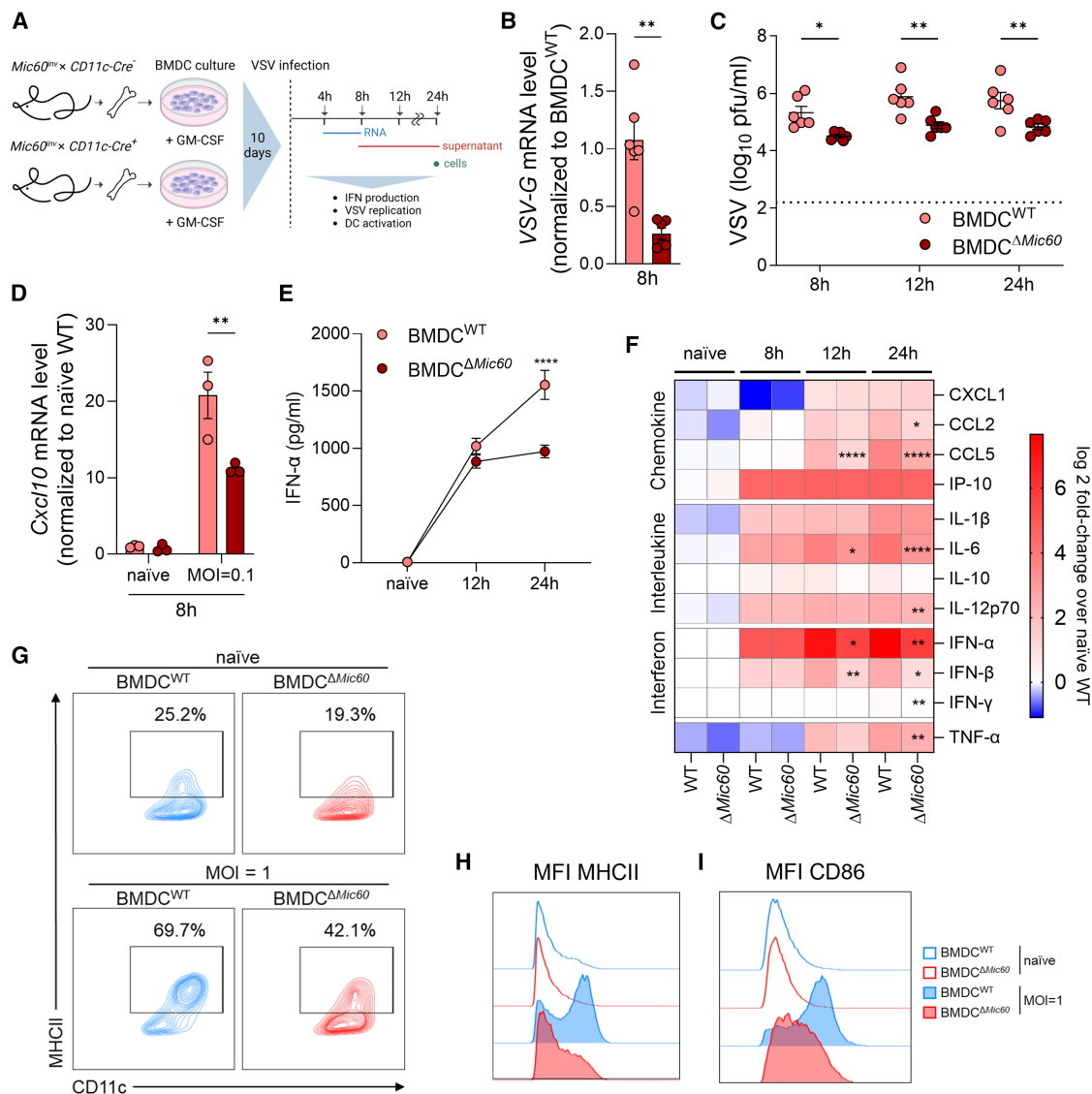


**Figure 5. MIC60 deficiency reduces VSV replication followed by limited immune responses in BMDCs**

(A) Schematic of experimental procedures to assess VSV infection and immune response in MIC60-competent or deficient BMDCs; illustration was made with Biorender.com.

(B) mRNA expression of VSV-G in MIC60-competent or deficient BMDCs at 8 h post infection at an MOI of 0.1; data from two experiments pooled with *n* = 6 mice per condition are shown. Significance was determined using two-tailed/unpaired Student's *t* test. \*\**p* < 0.01. Data are presented as mean ± SEM.

(C) VSV titer in the supernatant after VSV infection at an MOI of 1; data from two experiments pooled with *n* = 6 mice per condition are shown. *p* values were determined by ordinary two-way ANOVA followed by Sidak's multiple comparisons test. \**p* < 0.05, \*\**p* < 0.01. Data are presented as mean ± SEM.

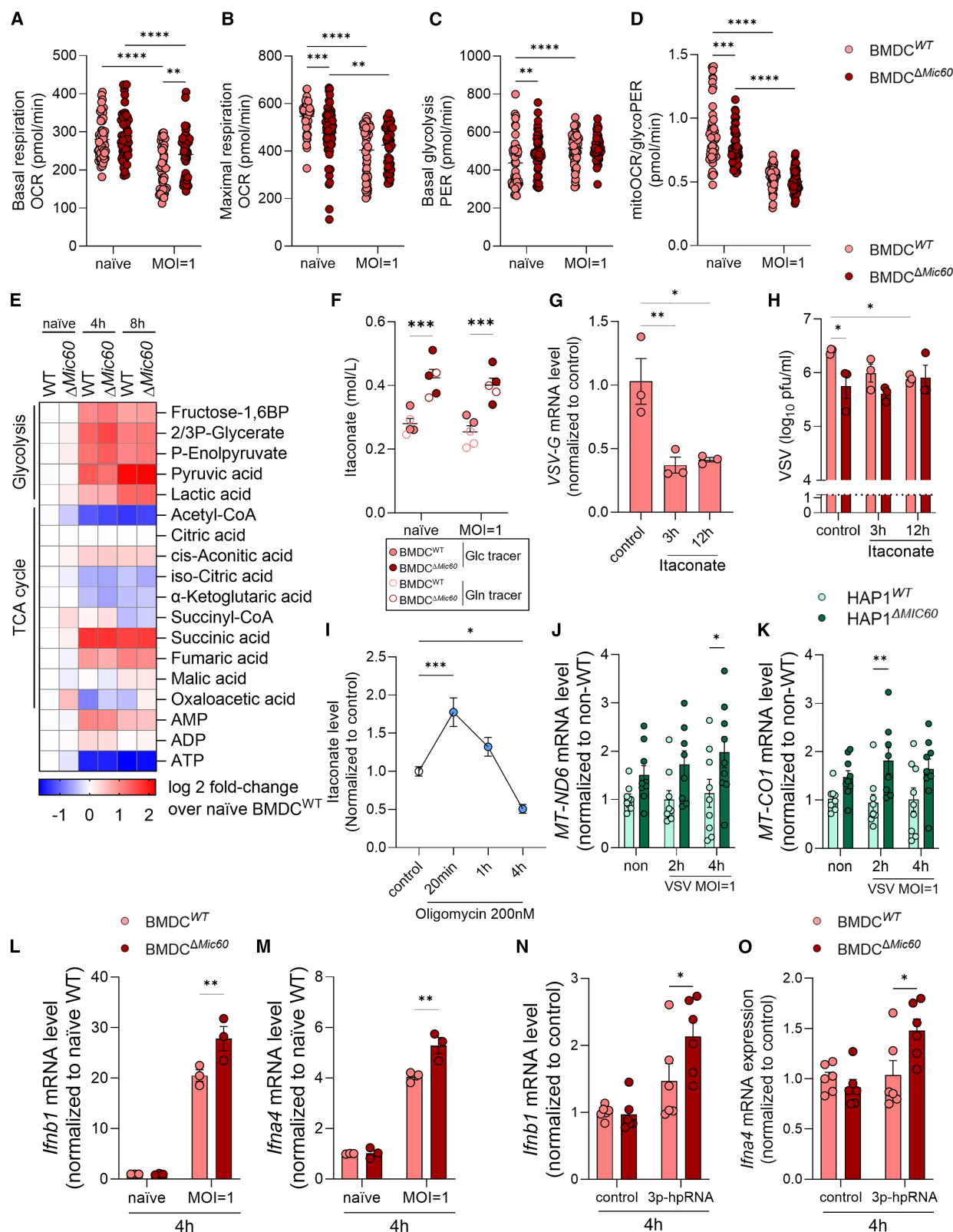
(D) *Cxcl10* mRNA expression in MIC60-competent or deficient BMDCs at 8 h post infection at an MOI of 0.1; data represent three biological replicates. Significance was determined by ordinary two-way ANOVA followed by Sidak's multiple comparisons test. \*\**p* < 0.01. Data are presented as mean ± SEM.

(E) IFN-α level in the supernatant of MIC60-competent or -deficient BMDCs after VSV infection at an MOI of 1; data from two experiments pooled with *n* = 6 mice per condition are shown. Statistical significance was determined using ordinary two-way ANOVA followed by Sidak's multiple comparisons test. \*\*\*\**p* < 0.0001. Data are presented as mean ± SEM.

(F) Cytokine and chemokine levels in the supernatant of MIC60-competent or deficient BMDCs after VSV infection at an MOI of 0.1; data from two experiments pooled with *n* = 6 mice per condition are shown. *p* values were determined by ordinary two-way ANOVA followed by Sidak's multiple comparisons test. \**p* < 0.05, \*\**p* < 0.01, \*\*\*\**p* < 0.0001.

(G and H) MIC60-competent or -deficient BMDCs were infected with VSV at MOI of 1 or remained naive, FACS analysis was conducted at 24 h post infection. (G) MHCII and CD11c expression in MIC60-competent or -deficient BMDCs; data are representative of three experiments pooled with *n* = 9 mice for naive and two experiments pooled with *n* = 6 mice for infected samples.

(H) Mean fluorescent intensity (MFI) of MHC-II and (I) CD86 in MIC60-competent or deficient BMDCs; data represent three experiments pooled with *n* = 9 mice for naive and two experiments pooled with *n* = 6 mice for infected samples.



(legend on next page)



synthase-consuming protons, while rotenone, antimycin, and uncouplers decrease MMP. It is difficult to distinguish the effect of disrupted IMM architecture from the effect of altered mitochondrial metabolism, since mitochondrial structure and metabolism are intricately linked in a dynamic equilibrium, mutually influencing each other to maintain cellular homeostasis. Based on these findings—as well as on our data discussed below using MIC60-deficient cells—we propose this structure-metabolic functional interplay to be critical for the observed anti-viral effects.

One major player that determines cristae architecture is the MICOS complex with its central subunit MIC60.<sup>36,45–47</sup> Loss of the MICOS complex results in impaired formation of CJs and cristae are usually arranged in multiple intramitochondrial stacks.<sup>3,4</sup> The  $F_1F_0$  ATP synthase, as well as the MICOS complex, are high-molecular-weight protein complexes located in the IMM that are also functionally linked and control membrane curvature in a coordinated and apparently dynamic manner.<sup>3,12,13,15,36</sup> We used MIC60-deficient cells, which exhibit a disrupted IMM architecture and showed reduced viral replication. We further validated and characterized the consequences in a mouse model lacking MIC60 in CD11-expressing cells, showing a reduced viral replication and immune activation after infection.

Several underlying molecular mechanisms by which MIC60-mediated cristae organization affects viral replication and modulates immune responses are possible. One obvious possibility is linked to alterations of mitochondrial metabolism either affecting OXPHOS directly and/or impairing metabolite transport across the inner membrane. Changes in metabolism are well possible, as virus replication and propagation often depend strongly on metabolic mechanisms of the host cell. Hence, viral infection with several viruses including hepatitis B virus, hepatitis C virus, HIV-1, and SARS-CoV-2 have been shown to result in

metabolic changes of host cells, particularly a switch to aerobic glycolysis.<sup>21</sup> Our data also indicate an increase in aerobic glycolysis after VSV infection; however, MIC60 did not grossly influence the switch to aerobic glycolysis or levels of AMP/ADP/ATP. Thus, we concluded that impaired cellular bioenergetics, which could explain the negative effects on viral replication, are not a major effect of MIC60 depletion. Still, cristae architecture may affect metabolism by altering metabolite transport across the inner membrane, possibly in a dynamic manner.<sup>3</sup> Interestingly, a metabolic gap of  $\alpha$ -KG, aspartate, and glutamine can result in limited viral replication.<sup>41–43</sup> While we did not observe delayed incorporation of  $^{13}\text{C}$  atoms in glutamine tracer experiments, we found increased oxaloacetic acid and itaconate levels in MIC60-deficient cells.

Recently, the relationship between specific metabolites and anti-viral effect or immune activation is attracting increased attention. Interestingly, it was reported that itaconate has anti-viral effects on a broad range of viruses including SARS-CoV-2, ZIKV, HSV1, and vaccinia virus.<sup>22,28,48</sup> Consistent with our data, during early viral infection, itaconate could increase type I IFN production in presence of PRR agonists.<sup>49</sup> It was also reported that enhanced type I IFN production after accumulation of itaconate is mediated by mtRNA release and sensing by intracellular PRRs in macrophages.<sup>29,30,33</sup> Notably, defects in the mitochondrial membrane organization can also increase mtDNA abundance in the cytosol, hence triggering increased expression of IFN-stimulated genes.<sup>31</sup> In our settings, we observed increased mtRNA levels in cytosol in MIC60-deficient HAP1 cells after VSV infection.

Taken together, in this paper we linked the IMM architecture and mitochondrial metabolism to viral infection. Furthermore, our findings reveal that MIC60 deficiency results in altered immune activation and reduced viral replication.

#### Figure 6. MIC60 deficiency alters cellular metabolism and results in accumulation of anti-viral itaconate in BMDCs

(A) Basal respiration, (B) maximal respiration, (C) basal glycolysis, and (D) ratio of mitoOCR to glycoPER in MIC60-competent or deficient BMDCs at 4 h post infection; data from three experiments pooled with  $n = 9$  mice in each group are shown.  $p$  values were determined using ordinary two-way ANOVA followed by uncorrected Fisher's least significant difference (LSD). \*\* $p < 0.01$ , \*\*\* $p < 0.001$ , \*\*\*\* $p < 0.0001$ . Data are represented as mean  $\pm$  SEM.

(E) MIC60-competent or deficient BMDCs were infected with VSV at MOI of 1. Heatmap showing the log<sub>2</sub> fold-changes of metabolites relating to glycolysis, TCA cycle and adenosine phosphates over naive WT BMDCs. BP, biphosphate; P-, phospho-; data are representative of three biological replicates.

(F) Itaconate concentration in WT or MIC60-deficient BMDCs; data were from glucose tracer (Glc) and glutamine tracer (Gln) experiments pooled with  $n = 3$  mice in each group.  $p$  values were determined by ordinary two-way ANOVA followed by Sidak's multiple comparisons test. \*\*\* $p < 0.001$ . Data are presented as mean  $\pm$  SEM.

(G and H) BMDCs were treated with 5 mM itaconate for 3 h or 12 h followed by VSV infection at an MOI of 1.

(G) mRNA expression of VSV-G in WT BMDCs at 4 h post infection.

(H) VSV titers in the supernatant at 8h post-infection; data are representative of three biological replicates.  $p$  values were determined using one-way ANOVA with Dunnett's multiple comparisons test (G) and ordinary two-way ANOVA followed by uncorrected Fisher's LSD (H). \* $p < 0.05$ , \*\* $p < 0.01$ . Data are presented as mean  $\pm$  SEM.

(I) BMDCs were treated with 200 nM oligomycin or vehicle. Itaconate concentrations per  $10^6$  cells were measured by ultra-performance liquid chromatography-tandem mass spectrometry at the indicated time points; data pooled with  $n = 3$  mice per condition and 2 technical replications per sample are shown. Significance was determined using one-way ANOVA with Dunnett's multiple comparisons test. \* $p < 0.05$ , \*\*\* $p < 0.001$ . Data are presented as mean  $\pm$  SEM.

(J and K) WT and MIC60-deficient HAP1 cells were infected with VSV at an MOI of 1 or remain non-infected, and cytosol fraction was extracted by digitonin. Cytosolic RNA levels of (J) *MT-ND6* and (K) *MT-CO1* were normalized by ACTB mRNA expression level in cytosol; data from three independent experiments are shown. Statistical significance was determined using ordinary two-way ANOVA followed by Sidak's multiple comparisons test. \* $p < 0.05$ , \*\* $p < 0.01$ . Data are presented as mean  $\pm$  SEM.

(L and M) MIC60-competent or deficient BMDCs were infected with VSV at an MOI of 1. mRNA expression of (L) *Ifnb1* and (M) *Ifna4* at 4 h post infection; data are representative of three biological replicates. Significance was determined by ordinary two-way ANOVA followed by Sidak's multiple comparisons test. \*\* $p < 0.01$ . Data are presented as mean  $\pm$  SEM.

(N and O) BMDCs were transfected with 3p-hpRNA (1  $\mu\text{g}/\text{mL}$ ) by jetPRIME for 4 h. mRNA expression of (N) *Ifnb1* and (O) *Ifna4* in WT or MIC60-deficient BMDCs; data from two experiments pooled with  $n = 6$  mice per condition are shown.  $p$  values were determined by ordinary two-way ANOVA followed by Sidak's multiple comparisons test. \* $p < 0.05$ . Data are presented as mean  $\pm$  SEM.



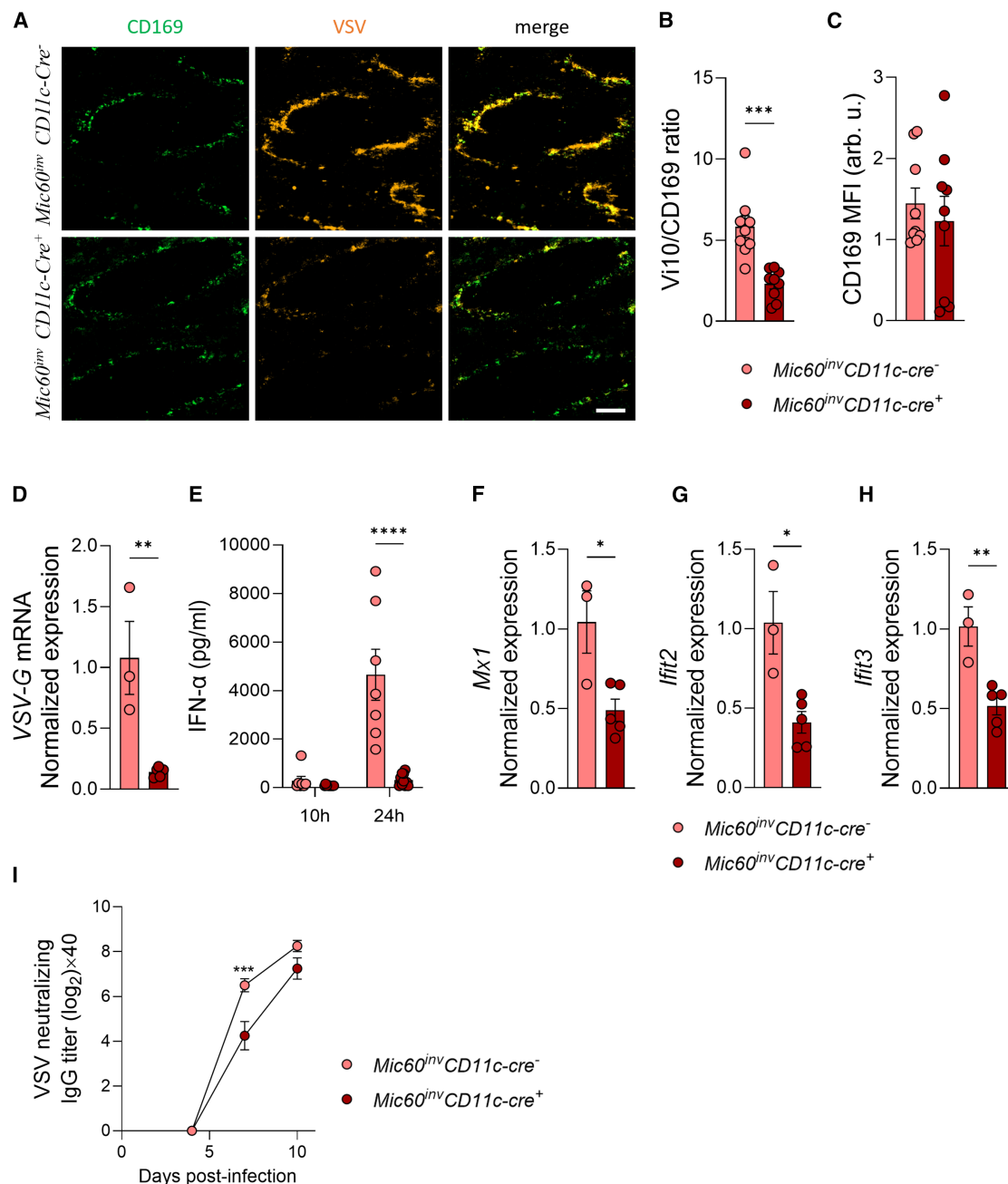


**Figure 7. MIC60 deficiency in CD11c-expressing cells reduces VSV replication in CD169<sup>+</sup> cells followed by reduced immune activation *in vivo***  
(A–C)  $Mic60^{inv/inv} \times CD11c-cre^+$  and  $Mic60^{inv/inv} \times CD11c-cre^-$  mice were infected intravenously with VSV at  $10^8$  pfu per mouse and spleen tissues were collected at 8 h post infection.

(A) Representative images showing localization of VSV-G and CD169; scale bar, 100  $\mu$ m.

(B and C) (B) Ratio of MFI of VSV-G to CD169 and (C) MFI of CD169; data are representative of three biological replicates. Statistical significance was determined using two-tailed/unpaired Student's t test. \*\*\* $p < 0.001$ . Data are represented as mean  $\pm$  SEM.

(D–I)  $Mic60^{inv/inv} \times CD11c-cre^+$  and  $Mic60^{inv/inv} \times CD11c-cre^-$  mice were infected intravenously with VSV at  $10^5$  pfu per mouse. (D) VSV-G mRNA levels in spleen, (E) IFN- $\alpha$  level in the serum, (F) *Mx1*, (G) *Ifit2*, and (H) *Ifit3* mRNA expression in spleen and (I) neutralizing IgG against VSV in the serum: data from  $n = 3$  mice in  $Mic60^{inv/inv} \times CD11c-cre^-$  mice and  $n = 5$  mice in  $Mic60^{inv/inv} \times CD11c-cre^+$  mice for (D–H) are shown. Data from  $n = 7$  mice in  $Mic60^{inv/inv} \times CD11c-cre^-$  group and  $n = 10$  mice in  $Mic60^{inv/inv} \times CD11c-cre^+$  group for (E), or from  $n = 4$  mice in each condition for (I) are shown.  $p$  values were determined using two-tailed/unpaired Student's t test (D–H) and ordinary two-way ANOVA followed by Sidak's multiple comparisons test (E and I). \* $p < 0.05$ , \*\* $p < 0.01$ , \*\*\* $p < 0.001$  and \*\*\*\* $p < 0.0001$ . Data are presented as mean  $\pm$  SEM.

## Limitations of the study

In the present, work we describe several consequences of altered cristae architecture including its contribution to anti-viral mechanisms resulting from altered mitochondrial metabolism, membrane potential, accumulation of itaconate, and release of mtRNA. However, the functional contributing consequences of the specific events to anti-viral activity or the potential overlapping effects of multiple events may vary depending on factors such as cell type and time point after infection as well as the degree and cause of mitochondrial membrane alteration. Therefore, at this point, it is not possible to generalize a single universal mechanism for the anti-viral effect of altered mitochondrial structure-metabolism. Furthermore, there are differences of immune sensors and properties between cell types such as HEK cells used for scRNA-seq and BMDCs used for characterization of MIC60 deficiency, possibly affecting the functionality of innate immune pathways. In addition, further differences in metabolite analyses using isotopic glucose and glutamine labeling might be time sensitive and require a more detailed analysis. Therefore, we cannot rule out that altered transport of metabolites between cytosol and mitochondrial compartments contributes to anti-viral effects observed in MIC60-deficient cells.

## RESOURCE AVAILABILITY

### Lead contact

Further information and requests for resources and reagents should be directed to the lead contact, Philipp A. Lang ([langp@uni-duesseldorf.de](mailto:langp@uni-duesseldorf.de)).

### Materials availability

This study did not generate new unique reagents.

### Data and code availability

- Original scRNA-seq and metabolomics data have been deposited at GEO and MetaboLights, respectively, and are publicly available as of the date of publication. Accession numbers are listed in the key resources table.
- This paper does not report original code.
- Any additional information required to reanalyze the data reported in this paper is available from the lead contact upon request.

## ACKNOWLEDGMENTS

We would like to thank D. Kolakofsky (University of Geneva) for providing VSV, the Centre for Information and Media Technology at Heinrich Heine University Düsseldorf for the Computational infrastructure and support, the Core Facility Electron Microscopy (CFEM) at the Medical faculty, Heinrich Heine University Düsseldorf for support on TEM and FIB-SEM imaging, the Center for Advanced imaging (CAi) at Heinrich Heine University Düsseldorf for confocal imaging and the LCSB Metabolomics and Lipidomics Platform for providing technical and analytical support on metabolic flux analysis. This study was supported by the German Research Foundation (DFG), RTG1949, LA2558/8-1, RE1575/4-1, RE1575/2-1, and XU160/3-1), the Jürgen Manchot Foundation (Molecules of Infection), the Volkswagen Foundation (9B797), the Christiane and Claudia Hempel Foundation, and the Medical Faculty of the Heinrich Heine University (Forschungskommission). Further support came from the German Research Foundation (DFG) under Germany's Excellence Strategy - EXC 2155 - project number 390874280. D.B. has been funded by Luxembourg National Research Fund (FNR)-CORE grant (C21/BM/15796788) and the Fondation Luxembourg (Treg HTS). A.A.P. acknowledges support from the Deutsche José Carreras Leukämie-Stiftung (DJCLS 18R/2021), the German Childhood Cancer Foundation (A2023/31), the German Federal Office for Radiation Protection (BfS), the DZIF (TTU

07-711), the German Ministry for Education and Research (Bundesministerium für Bildung und Forschung BMBF, grant no. 01KD2410A (EDI-4-ALL), the Medical Faculty of the Heinrich Heine University (Forschungskommission), and the Düsseldorf School of Oncology.

## AUTHOR CONTRIBUTIONS

I.K. designed and performed the experiments, analyzed the data, and wrote the manuscript. N.L. analyzed the data and wrote the manuscript. M.G. performed the experiments, discussed the data and wrote the manuscript. N.P. K., D.A., J.W., K.S.K., S.O., T.L., K.K., D.H., E.M., M.A., and A.K.B performed the experiments and analyzed the data. A.K.K., H.C.X., and A.A.P discussed the data and wrote the manuscript. T.K. and D.B. performed the experiments and analyzed and discussed the data. T.F. performed the experiment and wrote the manuscript. U.K. discussed the data. A.S.R. and P.A.L. initiated the study, planned and performed the experiments, discussed and analyzed the data, and wrote the manuscript.

## DECLARATION OF INTERESTS

The authors declare no competing interests.

## STAR★METHODS

Detailed methods are provided in the online version of this paper and include the following:

- **KEY RESOURCES TABLE**
- **EXPERIMENTAL MODEL AND STUDY PARTICIPANT DETAILS**
  - Ethics for animal experiments
  - Generation of Mic60 knockout mice
  - Cell models
  - Virus strain
  - Bone marrow-derived dendritic cells (BMDCs)
  - Human monocyte-derived dendritic cells (Mo-DCs)
- **METHOD DETAILS**
  - 10X Genomics library preparation and single cell RNA-sequencing
  - Differential expressed gene (DEG) and gene set enrichment analysis (GSEA)
  - Cellular respiration measurements after mitochondrial inhibitor treatment
  - RNA purification and real-time quantitative PCR
  - Determination of viral titer after treatment with ETC inhibitor
  - Determination of oligomerization state of  $F_1F_0$  ATP synthase by blue native PAGE
  - Transmission electron microscopy (TEM)
  - Focused ion beam scanning electron microscopy (FIB-SEM)
  - ELISA
  - Flow cytometry analysis
  - Oxygen consumption rate and extracellular acidification in BMDCs
  - Targeted metabolomics analysis by LC-MS/MS
  - Metabolic flux analysis and quantification of itaconate in BMDC
  - Digitonin fractionation for detection of cytosolic mtRNA
  - Histology
  - Quantification of neutralizing IgG
  - Measurement of VSV plaque formation after ETC inhibition
  - SARS-CoV-2 infection and CPE scoring
  - Western blotting
  - Quantification of cytosolic DNA foci
- **QUANTIFICATION AND STATISTICAL ANALYSIS**

## SUPPLEMENTAL INFORMATION

Supplemental information can be found online at <https://doi.org/10.1016/j.celrep.2025.115922>.

Received: July 8, 2024

Revised: April 3, 2025

Accepted: June 6, 2025

Published: July 7, 2025

## REFERENCES

- Tiku, V., Tan, M.W., and Dikic, I. (2020). Mitochondrial Functions in Infection and Immunity. *Trends Cell Biol.* 30, 263–275.
- Marchi, S., Guilbaud, E., Tait, S.W.G., Yamazaki, T., and Galluzzi, L. (2023). Mitochondrial control of inflammation. *Nat. Rev. Immunol.* 23, 159–173.
- Kondadi, A.K., Anand, R., and Reichert, A.S. (2020). Cristae Membrane Dynamics - A Paradigm Change. *Trends Cell Biol.* 30, 923–936.
- Kondadi, A.K., and Reichert, A.S. (2024). Mitochondrial Dynamics at Different Levels: From Cristae Dynamics to Interorganellar Cross Talk. *Annu. Rev. Biophys.* 53, 147–168.
- Zick, M., Rabl, R., and Reichert, A.S. (2009). Cristae formation-linking ultrastructure and function of mitochondria. *Biochim. Biophys. Acta* 1793, 5–19.
- Giacomello, M., Pyakurel, A., Glytsou, C., and Scorrano, L. (2020). The cell biology of mitochondrial membrane dynamics. *Nat. Rev. Mol. Cell Biol.* 21, 204–224.
- Frezza, C., Cipolat, S., Martins de Brito, O., Micaroni, M., Bezoussenko, G.V., Rudka, T., Bartoli, D., Polishuck, R.S., Danial, N.N., De Strooper, B., and Scorrano, L. (2006). OPA1 controls apoptotic cristae remodeling independently from mitochondrial fusion. *Cell* 126, 177–189.
- Paumard, P., Vaillier, J., Couly, B., Schaeffer, J., Soubannier, V., Mueller, D.M., Br  thes, D., di Rago, J.P., and Velours, J. (2002). The ATP synthase is involved in generating mitochondrial cristae morphology. *EMBO J.* 21, 221–230.
- Barrera, M., Koob, S., Dikov, D., Vogel, F., and Reichert, A.S. (2016). OPA1 functionally interacts with MIC60 but is dispensable for crista junction formation. *FEBS Lett.* 590, 3309–3322.
- Hessenberger, M., Zerbes, R.M., Rampelt, H., Kunz, S., Xavier, A.H., Purf  rst, B., Lilie, H., Pfanner, N., van der Laan, M., and Daumke, O. (2017). Regulated membrane remodeling by Mic60 controls formation of mitochondrial crista junctions. *Nat. Commun.* 8, 15258.
- Glytsou, C., Calvo, E., Cogliati, S., Mehrotra, A., Anastasia, I., Righi, G., Raimondi, A., Shintani, N., Loureiro, M., Vazquez, J., et al. (2016). Optic Atrophy 1 Is Epistatic to the Core MICOS Component MIC60 in Mitochondrial Cristae Shape Control. *Cell Rep.* 17, 3024–3034.
- Eydt, K., Davies, K.M., Behrendt, C., Wittig, I., and Reichert, A.S. (2017). Cristae architecture is determined by an interplay of the MICOS complex and the F1FO ATP synthase via Mic27 and Mic10. *Microb. Cell* 4, 259–272.
- Rampelt, H., Bohnert, M., Zerbes, R.M., Horvath, S.E., Warscheid, B., Pfanner, N., and van der Laan, M. (2017). Mic10, a Core Subunit of the Mitochondrial Contact Site and Cristae Organizing System, Interacts with the Dimeric F(1)F(o)-ATP Synthase. *J. Mol. Biol.* 429, 1162–1170.
- Kondadi, A.K., Anand, R., H  nsch, S., Urbach, J., Zobel, T., Wolf, D.M., Segawa, M., Liesa, M., Shiriha, O.S., Weidtkamp-Peters, S., and Reichert, A.S. (2020). Cristae undergo continuous cycles of membrane remodeling in a MICOS-dependent manner. *EMBO Rep.* 21, e49776.
- Rampelt, H., Wollweber, F., Licheva, M., de Boer, R., Perschil, I., Steidle, L., Becker, T., Bohnert, M., van der Klei, I., Kraft, C., et al. (2022). Dual role of Mic10 in mitochondrial cristae organization and ATP synthase-linked metabolic adaptation and respiratory growth. *Cell Rep.* 38, 110290.
- Gao, S., and Hu, J. (2021). Mitochondrial Fusion: The Machineries In and Out. *Trends Cell Biol.* 31, 62–74.
- Otera, H., Ishihara, N., and Mihara, K. (2013). New insights into the function and regulation of mitochondrial fission. *Biochim. Biophys. Acta* 1833, 1256–1268.
- Baker, N., Patel, J., and Khacho, M. (2019). Linking mitochondrial dynamics, cristae remodeling and supercomplex formation: How mitochondrial structure can regulate bioenergetics. *Mitochondrion (Amst.)* 49, 259–268.
- Tabara, L.C., Segawa, M., and Prudent, J. (2024). Molecular mechanisms of mitochondrial dynamics. *Nat. Rev. Mol. Cell Biol.* 26, 123–146.
- Saller, B.S., W  hrle, S., Fischer, L., Dufosse, C., Ingerl, I.L., Kessler, S., Mateo-Tortola, M., Gorka, O., Lange, F., Cheng, Y., et al. (2024). Acute suppression of mitochondrial ATP production prevents apoptosis and provides an essential signal for NLRP3 inflammasome activation. *Immunity (Camb., Mass.)* 58, 90–107.
- Foo, J., Bellot, G., Pervaiz, S., and Alonso, S. (2022). Mitochondria-mediated oxidative stress during viral infection. *Trends Microbiol.* 30, 679–692.
- Palmer, C.S. (2022). Innate metabolic responses against viral infections. *Nat. Metab.* 4, 1245–1259.
- Paludan, S.R., Pradeu, T., Masters, S.L., and Mogensen, T.H. (2021). Constitutive immune mechanisms: mediators of host defence and immune regulation. *Nat. Rev. Immunol.* 21, 137–150.
- Zecchini, V., Paupe, V., Herranz-Montoya, I., Janssen, J., Wortel, I.M.N., Morris, J.L., Ferguson, A., Chowdury, S.R., Segarra-Mondejar, M., Costa, A.S.H., et al. (2023). Fumarate induces vesicular release of mtDNA to drive innate immunity. *Nature* 615, 499–506.
- Peace, C.G., and O'Neill, L.A. (2022). The role of itaconate in host defense and inflammation. *J. Clin. Investig.* 132, e148548.
- Shi, X., Zhou, H., Wei, J., Mo, W., Li, Q., and Lv, X. (2022). The signaling pathways and therapeutic potential of itaconate to alleviate inflammation and oxidative stress in inflammatory diseases. *Redox Biol.* 58, 102553.
- Mills, E.L., Ryan, D.G., Prag, H.A., Dikovskaya, D., Menon, D., Zaslon, Z., Jedrychowski, M.P., Costa, A.S.H., Higgins, M., Hams, E., et al. (2018). Itaconate is an anti-inflammatory metabolite that activates Nrf2 via alkylation of KEAP1. *Nature* 556, 113–117.
- Daniels, B.P., Kofman, S.B., Smith, J.R., Norris, G.T., Snyder, A.G., Kolb, J.P., Gao, X., Locasale, J.W., Martinez, J., Gale, M., Jr., et al. (2019). The Nucleotide Sensor ZBP1 and Kinase RIPK3 Induce the Enzyme IRG1 to Promote an Antiviral Metabolic State in Neurons. *Immunity (Camb., Mass.)* 50, 64–76.
- West, A.P., Khoury-Hanold, W., Staron, M., Tal, M.C., Pineda, C.M., Lang, S.M., Bestwick, M., Duguay, B.A., Raimundo, N., MacDuff, D.A., et al. (2015). Mitochondrial DNA stress primes the antiviral innate immune response. *Nature* 520, 553–557.
- Dhir, A., Dhir, S., Borowski, L.S., Jimenez, L., Teitell, M., R  tig, A., Crow, Y.J., Rice, G.I., Duffy, D., Tamby, C., et al. (2018). Mitochondrial double-stranded RNA triggers antiviral signalling in humans. *Nature* 560, 238–242.
- He, B., Yu, H., Liu, S., Wan, H., Fu, S., Liu, S., Yang, J., Zhang, Z., Huang, H., Li, Q., et al. (2022). Mitochondrial cristae architecture protects against mtDNA release and inflammation. *Cell Rep.* 41, 111774.
- Hooftman, A., Peace, C.G., Ryan, D.G., Day, E.A., Yang, M., McGettrick, A.F., Yin, M., Montano, E.N., Huo, L., Toller-Kawahisa, J.E., et al. (2023). Macrophage fumarate hydratase restrains mtRNA-mediated interferon production. *Nature* 615, 490–498.
- O'Carroll, S.M., Peace, C.G., Toller-Kawahisa, J.E., Min, Y., Hooftman, A., Charki, S., Kehoe, L., O'Sullivan, M.J., Zoller, A., McGettrick, A.F., et al. (2024). Itaconate drives mtRNA-mediated type I interferon production through inhibition of succinate dehydrogenase. *Nat. Metab.* 11, 2060–2069.
- Campanella, M., Casswell, E., Chong, S., Farah, Z., Wieckowski, M.R., Abramov, A.Y., Tinker, A., and Duchon, M.R. (2008). Regulation of mitochondrial structure and function by the F1FO-ATPase inhibitor protein, IF1. *Cell Metab.* 8, 13–25.
- Davies, K.M., Anselmi, C., Wittig, I., Faraldo-G  mez, J.D., and K  hlbrandt, W. (2012). Structure of the yeast F1FO-ATP synthase dimer and its role in shaping the mitochondrial cristae. *Proc. Natl. Acad. Sci. USA* 109, 13602–13607.

# Cell Reports

## Article



36. Rabl, R., Soubannier, V., Scholz, R., Vogel, F., Mendl, N., Vasiljev-Neumeyer, A., Körner, C., Jagasia, R., Keil, T., Baumeister, W., et al. (2009). Formation of cristae and crista junctions in mitochondria depends on antagonism between Fc1j and Su e/g. *J. Cell Biol.* 185, 1047–1063.
37. Cogliati, S., Frezza, C., Soriano, M.E., Varanita, T., Quintana-Cabrera, R., Corrado, M., Cipolat, S., Costa, V., Casarin, A., Gomes, L.C., et al. (2013). Mitochondrial cristae shape determines respiratory chain supercomplexes assembly and respiratory efficiency. *Cell* 155, 160–171.
38. Golombek, M., Tsigaras, T., Schaumkessel, Y., Hänsch, S., Weidtkamp-Peters, S., Anand, R., Reichert, A.S., and Kondadi, A.K. (2024). Cristae dynamics is modulated in bioenergetically compromised mitochondria. *Life Sci. Alliance* 7, e202302386.
39. Honke, N., Shaabani, N., Cadeddu, G., Sorg, U.R., Zhang, D.E., Trilling, M., Klingel, K., Sauter, M., Kandolf, R., Gailus, N., et al. (2011). Enforced viral replication activates adaptive immunity and is essential for the control of a cytopathic virus. *Nat. Immunol.* 13, 51–57.
40. Xu, H.C., Wang, R., Shinde, P.V., Walotka, L., Huang, A., Poschmann, G., Huang, J., Liu, W., Stühler, K., Schaal, H., et al. (2021). Slow viral propagation during initial phase of infection leads to viral persistence in mice. *Commun. Biol.* 4, 508.
41. Codo, A.C., Davanzo, G.G., Monteiro, L.d.B., de Souza, G.F., Muraro, S. P., Virgilio-da-Silva, J.V., Prodonoff, J.S., Carregari, V.C., de Biagi Junior, C.A.O., Crunfli, F., et al. (2020). Elevated Glucose Levels Favor SARS-CoV-2 Infection and Monocyte Response through a HIF-1 $\alpha$ /Glycolysis-Dependent Axis. *Cell Metab.* 32, 437–446.
42. Wang, P., Xu, J., Wang, Y., and Cao, X. (2017). An interferon-independent lncRNA promotes viral replication by modulating cellular metabolism. *Science* 358, 1051–1055.
43. Thai, M., Thaker, S.K., Feng, J., Du, Y., Hu, H., Ting Wu, T., Graeber, T.G., Braas, D., and Christofk, H.R. (2015). MYC-induced reprogramming of glutamine catabolism supports optimal virus replication. *Nat. Commun.* 6, 8873.
44. Iannaccone, M., Moseman, E.A., Tonti, E., Bosurgi, L., Junt, T., Henrickson, S.E., Whelan, S.P., Guidotti, L.G., and von Andrian, U.H. (2010). Subcapsular sinus macrophages prevent CNS invasion on peripheral infection with a neurotropic virus. *Nature* 465, 1079–1083.
45. von der Malsburg, K., Müller, J.M., Bohnert, M., Oeljeklaus, S., Kwiatkowska, P., Becker, T., Loniewska-Lwowska, A., Wiese, S., Rao, S., Milenkovic, D., et al. (2011). Dual role of mitofilin in mitochondrial membrane organization and protein biogenesis. *Dev. Cell* 21, 694–707.
46. Hoppins, S., Collins, S.R., Cassidy-Stone, A., Hummel, E., Devay, R.M., Lackner, L.L., Westermann, B., Schuldiner, M., Weissman, J.S., and Nunari, J. (2011). A mitochondrial-focused genetic interaction map reveals a scaffold-like complex required for inner membrane organization in mitochondria. *J. Cell Biol.* 195, 323–340.
47. Harner, M., Körner, C., Walther, D., Mokranjac, D., Kaesmacher, J., Welsch, U., Griffith, J., Mann, M., Reggiori, F., and Neupert, W. (2011). The mitochondrial contact site complex, a determinant of mitochondrial architecture. *EMBO J.* 30, 4356–4370.
48. Olganier, D., Farahani, E., Thyrted, J., Blay-Cadanet, J., Herengt, A., Idorn, M., Hait, A., Hernaez, B., Knudsen, A., Iversen, M.B., et al. (2020). SARS-CoV2-mediated suppression of NRF2-signaling reveals potent antiviral and anti-inflammatory activity of 4-octyl-itaconate and dimethyl fumarate. *Nat. Commun.* 11, 4938.
49. Swain, A., Bambouskova, M., Kim, H., Andhey, P.S., Duncan, D., Auclair, K., Chubukov, V., Simons, D.M., Roddy, T.P., Stewart, K.M., and Artyomov, M.N. (2020). Comparative evaluation of itaconate and its derivatives reveals divergent inflammasome and type I interferon regulation in macrophages. *Nat. Metab.* 2, 594–602.
50. Hansen, J., Floss, T., Van Sloun, P., Füchtbauer, E.M., Vauti, F., Arnold, H. H., Schnütgen, F., Wurst, W., von Melchner, H., and Ruiz, P. (2003). A large-scale, gene-driven mutagenesis approach for the functional analysis of the mouse genome. *Proc. Natl. Acad. Sci. USA* 100, 9918–9922.
51. Schnütgen, F., De-Zolt, S., Van Sloun, P., Hollatz, M., Floss, T., Hansen, J., Altschmied, J., Seisenberger, C., Ghyselincx, N.B., Ruiz, P., et al. (2005). Genomewide production of multipurpose alleles for the functional analysis of the mouse genome. *Proc. Natl. Acad. Sci. USA* 102, 7221–7226.
52. Rodriguez, C.I., Buchholz, F., Galloway, J., Sequerra, R., Kasper, J., Ayala, R., Stewart, A.F., and Dymecki, S.M. (2000). High-efficiency deleter mice show that FLPe is an alternative to Cre-loxP. *Nat. Genet.* 25, 139–140.
53. Uez, N., Lickert, H., Kohlhasse, J., de Angelis, M.H., Kühn, R., Wurst, W., and Floss, T. (2008). Sall4 isoforms act during proximal-distal and anterior-posterior axis formation in the mouse embryo. *Genesis* 46, 463–477.
54. Caton, M.L., Smith-Raska, M.R., and Reizis, B. (2007). Notch-RBP-J signaling controls the homeostasis of CD8<sup>+</sup> dendritic cells in the spleen. *J. Exp. Med.* 204, 1653–1664.
55. Driggers, R.W., Ho, C.Y., Korhonen, E.M., Kuivanen, S., Jääskeläinen, A. J., Smura, T., Rosenberg, A., Hill, D.A., DeBiasi, R.L., Vezina, G., et al. (2016). Zika Virus Infection with Prolonged Maternal Viremia and Fetal Brain Abnormalities. *N. Engl. J. Med.* 374, 2142–2151.
56. Walker, A., Houwaart, T., Wienemann, T., Vasconcelos, M.K., Strelow, D., Senff, T., Hülse, L., Adams, O., Andree, M., Hauka, S., et al. (2020). Genetic structure of SARS-CoV-2 reflects clonal superspreading and multiple independent introduction events, North-Rhine Westphalia, Germany, February and March 2020. *Euro Surveill.* 25, 2000746.
57. Ramani, A., Müller, L., Ostermann, P.N., Gabriel, E., Abida-Islam, P., Müller-Schiffmann, A., Mariappan, A., Goureau, O., Gruell, H., Walker, A., et al. (2020). SARS-CoV-2 targets neurons of 3D human brain organoids. *EMBO J.* 39, e106230.
58. Lutz, M.B., Kukutsch, N., Ogilvie, A.L., Rössner, S., Koch, F., Romani, N., and Schuler, G. (1999). An advanced culture method for generating large quantities of highly pure dendritic cells from mouse bone marrow. *J. Immunol. Methods* 223, 77–92.
59. Sallusto, F., and Lanzavecchia, A. (1994). Efficient presentation of soluble antigen by cultured human dendritic cells is maintained by granulocyte/macrophage colony-stimulating factor plus interleukin 4 and downregulated by tumor necrosis factor  $\alpha$ . *J. Exp. Med.* 179, 1109–1118.
60. Aaltonen, M.J., Friedman, J.R., Osman, C., Salin, B., di Rago, J.P., Nunari, J., Langer, T., and Tatsuta, T. (2016). MICOS and phospholipid transfer by Ups2-Mdm35 organize membrane lipid synthesis in mitochondria. *J. Cell Biol.* 213, 525–534.
61. Traag, V.A., Waltman, L., and van Eck, N.J. (2019). From Louvain to Leiden: guaranteeing well-connected communities. *Sci. Rep.* 9, 5233.
62. Fang, Z., Liu, X., and Peltz, G. (2023). GSEAPy: a comprehensive package for performing gene set enrichment analysis in Python. *Bioinformatics* 39, btac757.
63. Shinde, P.V., Xu, H.C., Maney, S.K., Kloetgen, A., Namineni, S., Zhuang, Y., Honke, N., Shaabani, N., Bellora, N., Doerrenberg, M., et al. (2018). Tumor Necrosis Factor-Mediated Survival of CD169(+) Cells Promotes Immune Activation during Vesicular Stomatitis Virus Infection. *J. Virol.* 92, e0163717.
64. Hamel, R., Dejarnac, O., Wichit, S., Ekcharyawat, P., Neyret, A., Luplertlop, N., Perera-Lecoin, M., Surasombattapattana, P., Talignani, L., Thomas, F., et al. (2015). Biology of Zika Virus Infection in Human Skin Cells. *J. Virol.* 89, 8880–8896.
65. Lang, J., Bohn, P., Bhat, H., Jastrow, H., Walkenfort, B., Cansiz, F., Fink, J., Bauer, M., Olszewski, D., Ramos-Nascimento, A., et al. (2020). Acid ceramidase of macrophages traps herpes simplex virus in multivesicular bodies and protects from severe disease. *Nat. Commun.* 11, 1338.
66. Grusdat, M., McIlwain, D.R., Xu, H.C., Pozdeev, V.I., Knievel, J., Crome, S. Q., Robert-Tissot, C., Dress, R.J., Pandya, A.A., Speiser, D.E., et al. (2014). IRF4 and BATF are critical for CD8(+) T-cell function following infection with LCMV. *Cell Death Differ.* 21, 1050–1060.
67. Lang, P.A., Shaabani, N., Borkens, S., Honke, N., Scheu, S., Booth, S., Brenner, D., Meryk, A., Barthuber, C., Recher, M., et al. (2013). Reduced type I interferon production by dendritic cells and weakened antiviral

- immunity in patients with Wiskott-Aldrich syndrome protein deficiency. *J. Allergy Clin. Immunol.* **131**, 815–824.
68. Reynolds, E.S. (1963). The use of lead citrate at high pH as an electron-opaque stain in electron microscopy. *J. Cell Biol.* **17**, 208–212.
  69. Campos, C.G., Veras, H.C.T., de Aquino Ribeiro, J.A., Costa, P.P.K.G., Araújo, K.P., Rodrigues, C.M., de Almeida, J.R.M., and Abdelnur, P.V. (2017). New Protocol Based on UHPLC-MS/MS for Quantitation of Metabolites in Xylose-Fermenting Yeasts. *J. Am. Soc. Mass Spectrom.* **28**, 2646–2657.
  70. Marquis, B.J., Louks, H.P., Bose, C., Wolfe, R.R., and Singh, S.P. (2017). A New Derivatization Reagent for HPLC-MS Analysis of Biological Organic Acids. *Chromatographia (Wiesb.)* **80**, 1723–1732.
  71. Law, A.S., Hafen, P.S., and Brault, J.J. (2022). Liquid chromatography method for simultaneous quantification of ATP and its degradation products compatible with both UV-Vis and mass spectrometry. *J. Chromatogr. B Analyt. Technol. Biomed. Life Sci.* **1206**, 123351.
  72. Jones, A.E., Arias, N.J., Acevedo, A., Reddy, S.T., Divakaruni, A.S., and Meriwether, D. (2021). A Single LC-MS/MS Analysis to Quantify CoA Biosynthetic Intermediates and Short-Chain Acyl CoAs. *Metabolites* **11**, 468.
  73. Xu, H.C., Huang, J., Pandya, A.A., Pandey, P., Wang, R., Zhang, Z., Zhuang, Y., Gertzen, C.G.W., Münk, C., Herebian, D., et al. (2022). Single MHC-I Expression Promotes Virus-Induced Liver Immunopathology. *Hepatology* **6**, 1620–1633.
  74. Werner, J., Kronberg, R.M., Stachura, P., Ostermann, P.N., Müller, L., Schaal, H., Bhatia, S., Kather, J.N., Borkhardt, A., Pandya, A.A., et al. (2021). Deep Transfer Learning Approach for Automatic Recognition of Drug Toxicity and Inhibition of SARS-CoV-2. *Viruses* **13**, 610.



## STAR★METHODS

### KEY RESOURCES TABLE

REAGENT or RESOURCE	SOURCE	IDENTIFIER
<b>Antibodies</b>		
Anti VSV glycoprotein	Made in house	clone: Vi10
Anti Mouse CD11c, PE	eBioscience	Cat#12-0114-82; RRID:AB_465552
Anti Mouse MHC Class II, Alexa Fluor 700	eBioscience	Cat#56-5321-82; RRID:AB_494009
Anti Mouse CD86, BV510	BD Bioscience	Cat#563077; RRID:AB_2737991
Anti Mouse/Rat CD40, FITC	eBioscience	Cat#11-0402-85; RRID:AB_465030
Anti Mouse CD169, FITC	BIO-RAD	Cat#MC A884F
Anti Mouse DNA	Progen	Cat#61014; RRID:AB_2750935
Anti Mouse IgM, FITC	eBioscience	Cat#11-5890-85; RRID:AB_465293
Anti Mouse IgG, HRP	Abcam	Cat#ab6789; RRID:AB_955439
Anti Mouse CD16/CD32	eBioscience	Cat#14-0161-86; RRID:AB_467135
Anti Mitofilin (MIC60)	Abcam	Cat#Ab110329; RRID:AB_10859613
Anti Mouse immunoglobulins, HRP	Agilent Technologies	Cat#P0260; RRID:AB_2636929
Anti Mouse ATP5A	Abcam	Cat#ab14748; RRID:AB_301447
CD14 Microbeads, human	Miltenyi Biotec	Cat#130-050-201; RRID:AB_2665482
<b>Bacterial and virus strains</b>		
VSV (Indiana strain, Mudd-Summers isolate)	D. Kolakofsky (University of Geneva)	N/A
ZIKV-AF (MR766)	ATCC	N/A
ZIKV-AM (FB-GWUH-2016)	O. Vapalahti (University of Helsinki)	N/A
SARS-CoV-2	L. Müller, H. Schaal (University Hospital Düsseldorf)	EPI_ISL_425126
LCMV-WE	F. Lehmann-Grube (Heinrich Pette Institute)	N/A
HSV-F1	H. Hengel (Institute of Virology, Freiburg, Germany)	N/A
<b>Chemicals, peptides, and recombinant proteins</b>		
Oligomycin	Sigma	Cat#75751
Rotenone	EMD Millipore	Cat#557368
Antimycin A	Sigma	Cat#A8674
Narasin	MedChemExpress	Cat#HY-121410
Maduramycin ammonium	MedChemExpress	Cat#HY-N7071A
Salinomycin sodium salt	MedChemExpress	Cat#HY-17439
Nanchangmycin	MedChemExpress	Cat#HY-100528
Nigericin sodium salt	MedChemExpress	Cat#HY-100381
CCCP	Sigma	Cat#C2759
DAPI	Invitrogen	Cat#D1306
GM-CSF murine rec.	PAN BIOTECH	Cat#CB-2210002
Human GM-CSF	Miltenyi Biotec	Cat#130-093-862
Human IL-4	Miltenyi Biotec	Cat#130-093-915
Ficoll-Paque™ PREMIUM density gradient media	cytiva	Cat#17544202
Poly-L-lysine	Sigma	Cat#P4707
3p-hpRNA	InvivoGen	Cat#tlrl-hprna
jetPRIME	Polyplus	Cat#101000027
Itaconate	Sigma	Cat#I29204

(Continued on next page)

**Continued**

REAGENT or RESOURCE	SOURCE	IDENTIFIER
Annexin V, APC	ImmunoTools	Cat#31490016
7AAD	Invitrogen	Cat#00-6993-50
Mito Tracker Red CMXRos	Invitrogen	Cat#M7512
MitoSox Red mitochondrial superoxide indicator	Invitrogen	Cat#M36008
Image-iT TMRM Reagent	Invitrogen	Cat#I34361
Digitonin	Sigma	Cat#D141

**Critical commercial assays**

3' CellPlex Kit Set A	10× genomics	Cat#1000261
Chromium Single Cell 3' NextGEM Reagent Kit v3.1	10× genomics	Cat#1000268
Seahorse XF Cell Mito Stress Test Kit	Agilent Technologies	Cat#103015-100
Seahorse XF Glycolytic Rate Assay Kit	Agilent Technologies	Cat#103344-100
RNeasy Mini Kit	QIAGEN	Cat#74106
iTaq Universal SYBR Green One-Step Kit	BIO RAD	Cat#1725151
Mouse IFN alpha ELISA Kit	Invitrogen	Cat#BMS6027TEN
LEGENDplex MU Anti-Virus Response Panel	BioLegend	Cat#740622
Luminescent ATP Detection Assay Kit	abcam	Cat#ab113849

**Deposited data**

scRNA-seq data	This paper	GEO:GSE297187
Targeted metabolomics analysis by LC-MS/MS	This paper	MetaboLights:MTBLS12438
Metabolic flux analysis	This paper	MetaboLights:MTBLS12437

**Experimental models: Cell lines**

Human: HEK293 cells (ACC 305)	Leibnitz Institute DSMZ	N/A
Monkey: Vero cells (CCL-81)	ATCC	N/A
Human: HAP1 cells	Horizon	N/A
Human: MIC60 KO HAP1 cells	Horizon	N/A

**Experimental models: Organisms/strains**

Mouse: <i>Mic60</i> <sup>inv</sup> × CD11c-Cre	Prof. Thomas Floss	This paper
--	--------------------	------------

**Oligonucleotides**

Primers for qPCR, see Table S1		N/A
CD11c cre forward primer: CATTGGGCCAGCTAAACAT; R: CCCGGCAAACAGGTAGTTA	euofins Genomics	N/A
CD11c cre reverse primer: CCCGGCAAACAGGTAGTTA	euofins Genomics	N/A
<i>Mic60</i> <sup>inv</sup> forward primer: GCACTT CTTAGGCCATTACATTACAG; TACCCGTGTATCCAATAAACC;	euofins Genomics	N/A
<i>Mic60</i> <sup>inv</sup> reverse primer: GCAACTGAACTCAGCACCCAGAA	euofins Genomics	N/A

**Software and algorithms**

ImageJ	National Institutes of Health	<a href="https://imagej.net/ij/">https://imagej.net/ij/</a>
GraphPad Prism (v10.1)	GraphPad Software	graphpad.com
10X Genomics Cell Ranger software (v6.1.2)	10X genomics	10xgenomics.com
SmartSEM software	ZEISS	zeiss.com
ZEISS Atlas 5	ZEISS	zeiss.com
Amira Software (2021)	Thermo fisher Scientific	thermofisher.com

(Continued on next page)

Continued

REAGENT or RESOURCE	SOURCE	IDENTIFIER
QuantiStudio Design & Analysis software (v2.7.0)	Thermo fisher Scientific	thermofisher.com
FlowJo (v10)	BD	flowjo.com
MassLynx software (v4.2)	Waters	waters.com
TagetLynx XS software	Waters	waters.com
NIS-Elements F4.30.01 software	Nikon	nissoftware.net
Other		
10X Chromium Controller	10X genomics	N/A
NextSeq 2000	Illumina Inc.	N/A
BD FACS-Melody	BD	N/A
BD FACS Fortessa	BD	N/A
Seahorse XFe96 Analyzer	Agilent Technologies	N/A
Transmission electron microscopy H7100	Hitachi	N/A
FIB-SEM	ZEISS	N/A
QuantiStudio 5	Applied biosystems	N/A
UPLC I-Class	Waters	N/A
Xevo TQ-XS	Waters	N/A

EXPERIMENTAL MODEL AND STUDY PARTICIPANT DETAILS

Ethics for animal experiments

Experiments with mice were approved by the Landesamt für Natur, Umwelt und Verbraucherschutz Nordrhein-Westfalen (LANUV) and all experiments were in accordance with the German law for animal protection.

Generation of Mic60 knockout mice

*Mic60* (*Immt*)<sup>inv/inv</sup> mice were bred to *CD11c-Cre* mice to conditionally knockout *Mic60* in the antigen-presenting cells by applying a two-step breeding scheme. In the first step, the pre-conditional *Mic60* mouse model (*Mic60*(*Immt*)<sup>inv/+</sup>) was generated in tbv-2 embryonic stem cells<sup>50</sup> using the gene trap technology as described previously.<sup>51</sup> Initially, a *Mic60*<sup>gt</sup> strain was generated after the gene trap had inserted in the intron 1 of the *Mic60* (*IMMT*) gene locus *IMMT*<sup>GT(H001C10)WRST</sup>, MGI:3897023. The gene trap vector orientation (*Mic60*<sup>gt</sup>) was inverted in *Mic60*<sup>inv/inv</sup> mice by breeding the *Mic60*<sup>gt</sup> with a strain expressing the FLPe recombinase.<sup>52</sup> Genotyping of embryos from *Mic60*<sup>gt</sup> mice was conducted as previously described,<sup>53</sup> after removing the extra-embryonic tissue, the embryonic portion was treated in Lysis buffer (Promega) for at least 7 h at 55°C. PCR was carried out afterward using the following cycles and oligonucleotides: 1 × 4 min 94°C; 35 × 94°C 40sec, 56°C 30sec, 72°C 30sec; 1 × 72°C 10 min. Wild-type amplification was performed using the oligonucleotide sequences H001C10f-5'-TTTGTGCATGTGTGTGGATGAGC-3' and H001C10R - 5'-GAACC CAGTTCGGGTGGTGTAGG-3', mutant fragments were obtained with the same reverse primer but with the primer splirev1 5'-GCTAGCTTGCCAAACCTACAGGTGG -3' within the gene trap vector. In the second step, we crossed *Mic60*(*Immt*)<sup>inv/inv</sup> mice with mice harboring the *CD11c-cre* BAC transgene expressing the Cre recombinase under control of the *Cd11c* promoter/enhancer regions within the BAC transgene.<sup>54</sup> *Mic60*<sup>inv/inv</sup> × *CD11c-Cre*<sup>+</sup> mice were back-crossed to C57BL/6J for 10 generations to obtain an inbred mouse strain. The mice were bred in house in the Central Institution for Animal Research and Scientific Animal Welfare (ZETT) at the Heinrich-Heine-University Düsseldorf, Germany. The mice were maintained under specific pathogen-free conditions, including a controlled housing conditions (22°C, 55% humidity, 12:12h light: dark cycle). Animals had *ad libitum* access to autoclaved water and sterile rodent breeding chow. Experiments included both male and female mice aged 8–15 weeks, but sex-specific analyses were not performed. The influence of sex on the results was not assessed and remains a limitation.

Cell models

HEK293 cells (ACC 305) were acquired from Leibnitz Institute DSMZ without further authentication. These cells were cultured in Dulbecco's modified Eagle's medium (DMEM) supplemented with 10% Fetal Bovine Serum (FBS) and 1% Pen Strep Glutamine, and tested negative for mycoplasma contamination. Vero cells (CCL-81) were purchased from ATCC without further authentication. These cells were cultured in alpha MEM Eagle containing 5% FBS, 1% Pen Strep Glutamine. MIC60-competent or deficient HAP1 cells were purchased from Horizon and deletion of MIC60 was confirmed by western blotting. These cells were maintained in Iscove's modified Dulbecco's medium (IMDM) containing 20% FBS, 1% Pen Strep and 1% Glutamax. All cells were kept at

37°C in an atmosphere of 5% CO<sub>2</sub> and subcultured 2–3 times per week and used for the experiment when they reached 90–95% confluence. Vero cells and HAP1 cells were not tested for mycoplasma contamination during this study.

### **Virus strain**

VSV (Indiana strain, Mudd-Summers isolate) was obtained from D. Kolakofsky (University of Geneva), and propagated on BHK-21 hamster kidney fibroblasts at a multiplicity of infection of 0.01. ZIKV-AF (MR766) was purchased from ATCC, and ZIKV-AM (FB-GWUH-2016) was obtained from Dr. Vapalahti.<sup>55</sup> ZIKV was propagated on *Aedes albopictus* C6/36 cells. SARS-CoV-2 was used as described previously (Sequence Accession Number: EPI\_ISL\_425126),<sup>56,57</sup> and propagated on Vero cells at MOI of 0.001. LCMV-WE strain was originally obtained from F. Lehmann-Grube (Heinrich Pette Institute) and propagated on L929 cells at MOI of 0.01. HSV-F1 was originally obtained from Prof. Hartmut Hengel (Institute of Virology, Freiburg, Germany) and propagated on BHK-21 cells at MOI of 0.001.

### **Bone marrow-derived dendritic cells (BMDCs)**

BMDCs were cultured as described before.<sup>40,58</sup> Bone marrow cells were flushed from femurs and tibias. The cells were seeded at a concentration of  $2 \times 10^6$  cells/10 mL in tissue-culture plates and differentiated with GM-CSF (40 ng/mL) in RPMI1640 containing 10% FBS, 1% Pen Strep Glutamine and 1 mM beta-mercaptoethanol with a medium change on day 3, 6, and 8. BMDCs were harvested on day 10 for the experiments. BMDCs were treated with 5 mM of itaconate for 3 or 12h. Itaconate was prepared as 125 mM stock solutions in the culture media. Of note, the cells were incubated with VSV for 2h without itaconate so that changes in acidity does not interfere with the viral entry. After inoculation with VSV, cells were kept in the presence of 5 mM itaconate for the indicated time points.

### **Human monocyte-derived dendritic cells (Mo-DCs)**

Mo-DCs were cultured as described before.<sup>59</sup> PBMCs were prepared from buffy coat using Ficoll-Paque density gradient media. CD14<sup>+</sup> monocytes were isolated by MACS isolation system, and cultured in RPMI1640 containing 10% FBS, 1% Pen Strep Glutamine and 1 mM beta-mercaptoethanol, supplemented with human GM-CSF (50 ng/mL) and IL4 (25 ng/mL) for 6 days.

## **METHOD DETAILS**

### **10X Genomics library preparation and single cell RNA-sequencing**

HEK cells were divided into 6 samples, three control samples and three samples infected with VSV at MOI = 0.1 for 4h ( $10^6$  cells per sample). Cells were labeled with 3' CellPlex Kit following manufacturer's protocol, and the samples from the same treatment group were pooled together. Viable cells were enriched by BD FACS-Melody. Single cell suspensions were used as input for the single cell droplet libraries generation on the 10X Chromium Controller system utilizing the Chromium Single Cell 3' NextGEM Reagent Kit v3.1 according to manufacturer's protocol. Sequencing was carried out on a NextSeq 2000 system (Illumina Inc. San Diego, USA) with a mean sequencing depth of 45,000 reads/cell. Raw sequencing data were processed using the 10X Genomics CellRanger software (v6.1.2). Raw BCL-files were demultiplexed and processed to Fastq-files using the CellRanger *mkfastq* pipeline. Alignment of reads to the mm10 genome, UMI counting as well as sample demultiplexing were performed via the CellRanger *multi* pipeline to generate a gene-barcode matrix. The Cellranger *aggr* pipeline was used for aggregation and sequencing depth normalization. Quality control, preprocessing and analysis of single cell RNA-sequencing data were performed using the python package Scanpy.<sup>60</sup> During quality control, cells were removed when they contain less than 400 genes, less than 3,500 reads, more than 100,000 reads or over 10% of mitochondrial genes to total transcripts. In addition, genes expressed in less than three cells were also removed. After the quality control, 7,358 cells of the naive sample, 11,869 cells of the VSV exposed sample, and 30,949 genes remained for analysis. The total gene count per barcode was normalized to 10,000 reads and reads were transformed to  $\log(x+1)$ . Lastly, count depth effects were regressed out and gene counts were scaled to unit variance and zero mean. Principal component analysis was carried out using the 2,000 most variable genes. For clustering and visualization, we calculated a Uniform Manifold Approximation and Projection for Dimension Reduction (UMAP) representation. Clusters were detected using the Leiden algorithm<sup>61</sup> with a resolution of 0.7.

### **Differential expressed gene (DEG) and gene set enrichment analysis (GSEA)**

Differential expressed gene (DEG) analysis was performed using the Wilcoxon rank-sum test and Bonferroni correction. Genes were removed when the log-fold change is between  $-0.25$  and  $0.25$ , the adjusted  $p$ -value  $\geq 0.01$  and the gene was detected in less than 25% in both groups in the comparison. Gene set enrichment analysis (GSEA) was performed using the python package Gseapy<sup>62</sup> with the biological process (GO:0008150) and cellular component (GO:0005575) gene set of the Gene Ontology database. For this analysis, genes were pre-ranked according to their  $p$ -value and log-fold change.

### **Cellular respiration measurements after mitochondrial inhibitor treatment**

Vero cells were seeded into Seahorse XF96 cell culture plate at a density of 20,000 cells per well and incubated overnight under standard culture conditions. Next day, cells were pre-treated with oligomycin or rotenone/antimycin A at the indicated concentration for 20 min. Cells were subsequently washed and incubated with Seahorse XF RPMI Medium containing 10 mM Glucose, 1 mM Pyruvate



and 2 mM L-Glutamine at 37°C in non-CO<sub>2</sub> incubator 1h prior to the measurement. Mitochondrial respiration function was measured using Seahorse XF Cell Mito Stress Test Kit according to the manufacturer's instructions.

### RNA purification and real-time quantitative PCR

Cells and spleen tissues were lysed in RLT buffer included in RNeasy Mini Kit (QIAGEN). RNA purification was conducted according to the manufacturer's instructions. Gene expression was measured using iTaq Universal SYBR Green One-Step Kit (BIO-RAD) and QuantiStudio 5 (Applied Biosystems). The acquired Ct values were normalized by the Ct value of *Gapdh* and analyzed based on the  $\Delta\Delta Ct$  method.

### Determination of viral titer after treatment with ETC inhibitor

Monolayers of Vero cells were prepared on 24-well plates one day prior to the treatment. Vero cells were treated with ETC inhibitors for 20 min, followed by inoculation with viruses. The input viral particles were washed at 1h (VSV and ZIKV) or 3h (LCMV and HSV) post-infection, and fresh medium containing the ETC inhibitors were added. Viral titers in the infected supernatants were determined by plaque assay on Vero cells in case of VSV,<sup>63</sup> ZIKV<sup>64</sup> and HSV.<sup>65</sup> In case of LCMV, the virus titers were determined using MC57G cells as described before.<sup>66,67</sup>

### Determination of oligomerization state of F<sub>1</sub>F<sub>0</sub> ATP synthase by blue native PAGE

HEK cells were grown on 15 cm dishes and were treated with the respective compounds once 80% confluence was reached. The cells were then washed with cold PBS, scraped and centrifuged at 900×g for 5 min at 4°C. The resulting cell pellets were resuspended in 1 mL of isotonic buffer containing 210 mM mannitol, 70 mM sucrose, 1 mM EDTA, 20 mM HEPES, 0.1% BSA, 1×protease inhibitor. After incubation on ice for 10 min, the cells were disrupted using a syringe and 20G cannula. Sequential centrifugation steps at 1,000×g for 10 min at 4°C were used to remove cell debris and to isolate mitochondria. Followed by a centrifugation at 10,000×g for 15 min at 4°C to pellet the mitochondria. Subsequently 100 μg of isolated mitochondria were solubilized for 1 h on ice using a digitonin-to-protein ratio of 2.5 g/g. To remove any insoluble material the samples were centrifuged at 20,000×g for 20 min at 4°C. The supernatants were then mixed with loading buffer (50% glycerol, 8 g/g Coomassie:detergent ratio) and loaded onto a 3–13% gradient gel. A voltage of 150 V and a current of 15 mA were applied for 16 h. The proteins were then transferred to a PVDF membrane and blocked in 5% milk in TBS-T overnight at 4°C. To identify the oligomerization/dimerization rate of the F<sub>1</sub>F<sub>0</sub> ATP synthase, the membranes were incubated with the ATP5A (1:1,000) antibody, and goat anti-mouse IgG (1:10,000) conjugated to HRP. Chemiluminescence signals were detected by Fusion-FX7 EDGE imaging system with the addition of SuperSignal West Pico PLUS.

### Transmission electron microscopy (TEM)

The cell pellets were fixed using 4% paraformaldehyde, 2.5% glutaraldehyde in 0.1% sodium cacodylate buffer (pH 7.4), and subsequently embedded in a droplet of 3% low melt agarose. The pellets were stained with 1% osmium tetroxide for 1h and with 1% uranyl acetate/1% phosphotungstic acid for 1h. The samples were dehydrated with graded ethanol series, embedding in Spurr's resin and polymerization at 70°C for 8h. The ultrathin sections (70nm) were cut with Ultracut EM UC7 (Leica, Wetzlar, Germany) and transferred to 200 mesh copper grids. These were stained with 1.5% uranyl acetate for 30 min, and with lead citrate for 8 min.<sup>68</sup> The images were acquired using a transmission electron microscope H7100 (Hitachi, Tokyo, Japan) at 100kV, with a Morada camera (EMSIS GmbH, Münster, Germany), and analyzed with ImageJ software.

### Focused ion beam scanning electron microscopy (FIB-SEM)

The embedded cell pellet samples used for TEM measurements were also processed for FIB-SEM (Crossbeam 550, Carl Zeiss AG). The pre-cut resin blocks were glued onto SEM aluminum stubs using conductive silver paste. The surface was coated with 25 nm-thick gold layer (108 auto, Cressington Scientific Instruments, Watford, UK). Screening for cells was performed with SmartSEM software package (Carl Zeiss AG, version 6.07) at an accelerating voltage of 15 kV (working distance 5 mm, SE2 detector). For image acquisition and 3D reconstruction, Zeiss Atlas 5 (Carl Zeiss AG, software version 5.3.5.3) was used. For MIC60-competent HAP1 cells after VSV infection, the image acquisition was done with gallium ion beam: 30 kV/1.5 nA, slice thickness: 25 nm, electron beam: 2 kV/2nA, field of view: 46.08 μm, pixel size: 20 nm and dwell time: 0.5 μm with line average of 11. For MIC60-deficient HAP1 cells after VSV infection, system parameters were the following: gallium ion beam: 30 kV/700 pA, slice thickness: 25 nm, electron beam: 2 kV/2nA, field of view: 49.6 μm, pixel size: 25 nm and dwell time: 0.5 μm with line average of 11. For both samples SE2 and inLens detector were used. The alignment and exportation of Image Stacks were carried out utilizing the Zeiss Atlas 5 software suite. Subsequently, these images were imported into the ThermoFisher Amira 2021 software. The reconstruction of individual mitochondria was accomplished through manual segmentation of organelles in 2D, culminating in the generation of a 3D model. A minimum of 8 mitochondria per cell were subjected to the reconstruction process. Using the same software, the surface area and volume of each mitochondrion were computed, followed by the calculation of an average values for every mitochondrion per cell. The surface area-to-volume ratio was calculated for each cell.

## ELISA

IFN $\alpha$  concentration in the serum and supernatant from infected cells was measured according to the manufacture's instruction.

## Flow cytometry analysis

Experiments were performed using a FACS Fortessa and analyzed using FlowJo software. For DCs staining, single suspensions of cells were incubated with antibodies (anti-MHC-II, CD11c, CD86 and CD40) for 30 min at 4°C. For the LEGENDplex assay, the supernatants from infected BMDCs were prepared in accordance with manufacturer's instruction.

## Oxygen consumption rate and extracellular acidification in BMDCs

BMDCs were seeded into XF96 well plate pre-coated with poly-L-lysine at  $2 \times 10^5$  cells per well followed by mock or VSV infection for 4h. Prior to the measurement, cells were washed once and kept in Seahorse XF RPMI Medium containing 10 mM Glucose, 1 mM Pyruvate and 2 mM L-Glutamine during the measurement. Mitochondrial respiration function was measured by Seahorse XF Cell Mito Stress Test Kit and glycolysis function was measured using Seahorse XF Glycolytic Rate Assay Kit according to the manufacturer's instructions.

## Targeted metabolomics analysis by LC-MS/MS

Extraction of the targeted metabolites was performed by adding 300  $\mu$ L Methanol/H<sub>2</sub>O (80/20; v/v) to the  $10^6$  cells, which were homogenized by ceramic beads CK14 using Precellys lysing kit (Bertin technologies). The corresponding isotopically labeled internal standards were added to the extraction solution. The targeted compounds were analyzed by UPLC-MS/MS. The system comprised a UPLC I-Class (Waters) coupled to a tandem mass spectrometer Xevo TQ-XS (Waters). Electrospray ionization was performed in the negative ionization mode for the compounds fructose-1,6-bisphosphate, phosphoenolpyruvate (PEP), 2/3-phosphoglycerate and itaconate.<sup>69</sup> The TCA, energy metabolites (AMP, ADP and ATP) as well acetyl- and succinyl-CoA were measured in the positive ionization mode as referred in the literature.<sup>70–72</sup> Mass spectrometric quantitation of the compounds was carried out in the multiple reaction monitoring (MRM) mode. MassLynx software (v4.2; Waters, UK) was used for instrument's control and data acquisition. Quantitation analysis was performed by TargetLynx XS software (Waters, UK).

## Metabolic flux analysis and quantification of itaconate in BMDC

Five million BMDCs were resuspended in 800  $\mu$ L of tracing media prepared as SILAC RPMI 1640 (Gibco) supplemented with 10% dialyzed FBS (US origin, Merck, F392-100ML), 1% penicillin/streptomycin (Gibco), L-arginine (Sigma-Aldrich), L-lysine (Sigma-Aldrich), and [1,2-<sup>13</sup>C] glucose (11.1mmol/L; Sigma-Aldrich) or [U-<sup>13</sup>C] glutamine isotopic tracers (2mmol/L; Cambridge Isotope Laboratories). The BMDCs were incubated for 2 h followed by mock or VSV infection (MOI = 1) for 4 h. Cells were then centrifuged for 5 min at 300 $\times$ g at room temperature. The cell pellets were then washed with 0.9% NaCl and centrifuged. The pellets were dissociated in 600  $\mu$ L of ice-cold H<sub>2</sub>O/methanol/chloroform (200  $\mu$ L each) and mixed on a shaker for 20 min at 4°C. The tubes were centrifuged at 17000 $\times$ g for 5 min at 4°C, and the resultant polar metabolite fraction was collected and stored at –80°C until the samples were processed further. The extracted metabolites were dried and subjected to further analytical pre-processing, including derivatization. Subsequent measurements were conducted on a GC-MS equipped with a 35MS analytical column. The analysis was performed with MetaboliteDetector software, which generated mass isotopomer distributions (MIDs) and semi-quantitative values. Outliers were removed based on internal standard deviations or peak shapes to ensure data integrity and reliability.

## Digitonin fractionation for detection of cytosolic mtRNA

Cytosolic fractionation was conducted as described before.<sup>24</sup>  $10^6$  Cells were washed once with PBS following fractionation by 25  $\mu$ g/mL of digitonin in isolation buffer (150mM NaCl and 50 mM HEPES) for 10 min at 4°C. The samples were then centrifuged for 10 min at 2,000 $\times$ g at 4°C. The supernatants were collected for RNA isolation. Cytosolic mtRNA levels were normalized by ACTB mRNA expression levels.

## Histology

Histological analysis of snap frozen tissue was performed as previously described.<sup>63,73</sup> Monoclonal antibody against VSV glycoprotein (Vi10; made in-house) was conjugated with Cy3 (abcam). CD169-expressing cells were stained with anti-CD169 PerCP antibody. Images were acquired by ZEISS Axio Observer Z1, and MFI was analyzed with ImageJ.

## Quantification of neutralizing IgG

Neutralizing antibody against VSV was measured as described before.<sup>63</sup> Diluted serum (1:40) was incubated for 30 min at 56°C for complement inactivation, and treated with beta-mercaptoethanol (0.1 M) for removal of IgM. Serum was titrated 1:2 over 12 steps and incubated with 1000 PFU of VSV. After 90 min of incubation, the virus-serum mixture was plaqued on Vero cells and overlay was added after 1h. Plaques were visualized after 24 h by crystal violet staining.<sup>63</sup>

### Measurement of VSV plaque formation after ETC inhibition

Vero cells were seeded into 96-well plate at a density of 30,000 cells per well and incubated overnight under standard culture conditions. Next day, cells were treated with oligomycin or rotenone/antimycin A at the indicated concentration for 20 min followed by VSV infection at  $\text{MOI} = 6 \times 10^{-4}$ . At 2h post-infection, overlay containing 2% methylcellulose in DMEM was added in each well to stop virus spreading. Plaques were visualized 24h later by crystal violet staining.

### SARS-CoV-2 infection and CPE scoring

Vero cells were seeded at a density of 30,000 cells per well in a 96-well plate one day prior to infection. Next day, the medium was changed to cell culture medium containing different dilutions of oligomycin, antimycin A or rotenone in a 11 serial 3-fold dilution. The cells were infected 20 min later with SARS-CoV-2 at  $\text{MOI}$  of 0.03. An overlay composed of DMEM with 1% methylcellulose was added at 2h post-infection. Images were taken with NIS-Elements F4.30.01 software 3 days after the infection, and quantified using deep transfer learning as previously described.<sup>74</sup> ResNet18 was retrained to classify SARS-CoV-2-infected cell cultures. For recognizing CPE and toxic effects (TOX), 'CPETOXnet' with three different classifications (CPE, TOX, and no CPE) was used.

### Western blotting

Total protein was extracted from MIC60-competent or deficient BMDCs and 15  $\mu\text{g}$  of protein was loaded on 10% (w/v) SDS-polyacrylamide gel. The protein samples were transferred to nitrocellulose membranes and incubated with anti-Mitofilin/MIC60 (clone 2E4AD5). Then anti-mouse immunoglobulin antibody conjugated with HRP were incubated after washing the primary antibody. HRP chemiluminescence was measured by Fusion-FX7 EDGE imaging system (Vilber Lourmat) with the addition of SuperSignal West Femto. Ponceau S served as loading control.

### Quantification of cytosolic DNA foci

BMDCs were incubated on cover glasses (No.1.5H) for 3h at 37°C followed by VSV infection at  $\text{MOI} = 1$  for 4h. After the infection, BMDCs were stained with 300 nM of Mito Tracker Red CMXRos for 30 min at 37°C. Then BMDCs were fixed in 4% PFA, followed by permeabilization with 0.1% Triton X-. After blocking overnight at 4°C with 10% FCS in PBS, Fc receptors were blocked by anti-CD16/CD32 antibody (1:50 dilution in 1% FCS). DNA was stained with mouse anti-DNA antibody and anti-mouse IgM antibody conjugated with FITC. Cells were then mounted on slides with fluorescence mounting medium (Dako) and imaged using Leica TCS SP8 STED3X microscope. Same acquisition settings were applied for all the samples. Approximately 30 BMDCs per mouse were imaged with ROI size of  $62.47 \mu\text{m} \times 62.47 \mu\text{m}$  at resolution of 38 nm/pixel. Four stacks of 332.4 nm per slice were obtained and processed with the Leica Lightning deconvolution module. Cytosolic DNA foci were counted manually and considered as cytosolic DNA foci when they are not co-localized with mitochondria.

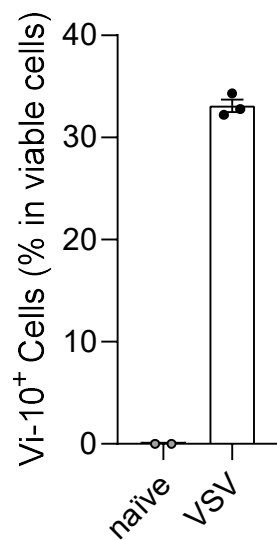
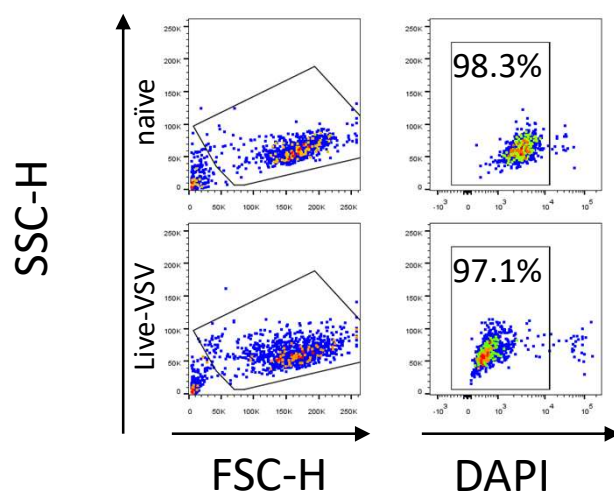
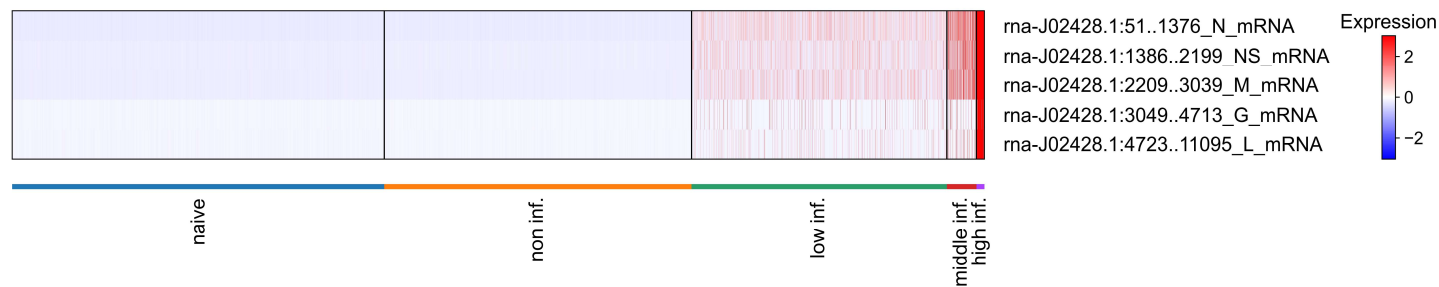
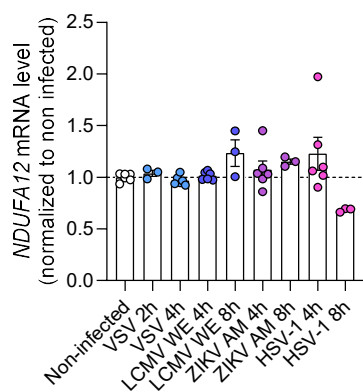
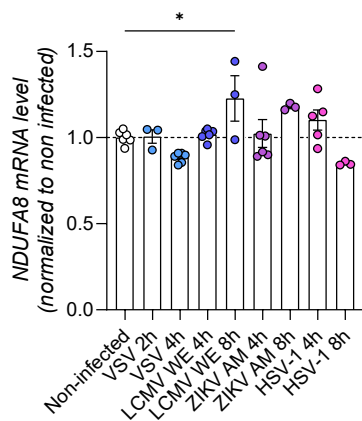
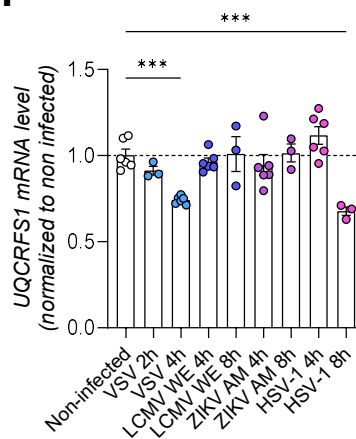
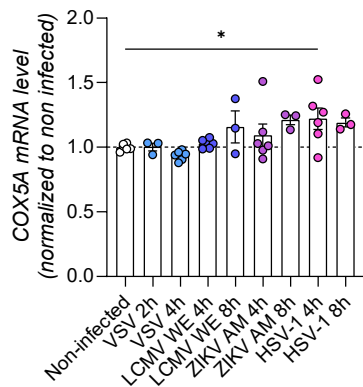
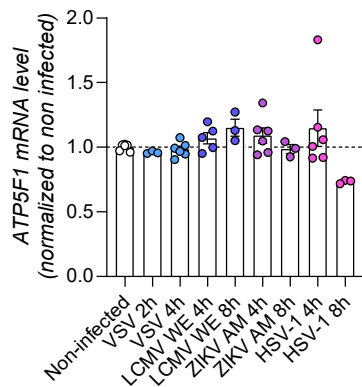
### QUANTIFICATION AND STATISTICAL ANALYSIS

Statistical analysis was performed using GraphPad Prism 10.1 (GraphPad Software). Data are expressed as mean  $\pm$  S.E.M. For analysis of statistical significance between two groups, a Student t-test was used. For multiple comparisons involving one variable, one-way ANOVA was performed. For simultaneous analysis of two variables among multiple groups was performed by two-way ANOVA. \* $p < 0.05$ , \*\* $p < 0.01$ , \*\*\* $p < 0.001$  and \*\*\*\* $p < 0.0001$  were considered statistically significant.

## **Supplemental information**

### **Controlling mitochondrial membrane architecture via MIC60 determines viral replication to promote anti-viral immunity**

**Ichiro Katahira, Nina Liebrand, Michal Gorzkiewicz, Niklas Paul Klahm, Džiuljeta Abromavičiūtė, Julia Werner, Karina Stephanie Krings, Sarah Orywol, Tobias Lautwein, Karl Köhrer, Diran Herebian, Ertan Mayatepek, Max Anstötz, Ann Kathrin Bergmann, Arun Kumar Kondadi, Haifeng C. Xu, Aleksandra A. Pandyra, Takumi Kobayashi, Dirk Brenner, Thomas Floss, Ulrich Kalinke, Andreas S. Reichert, and Philipp A. Lang**

**A****B****C****D****E****F****G****H**



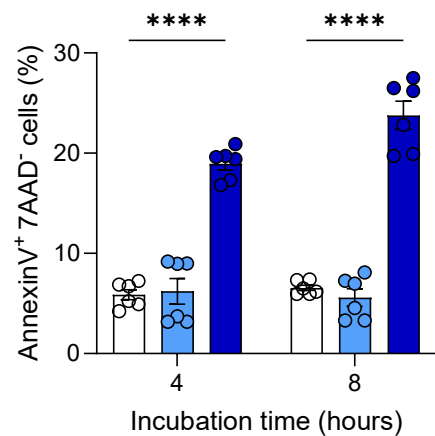
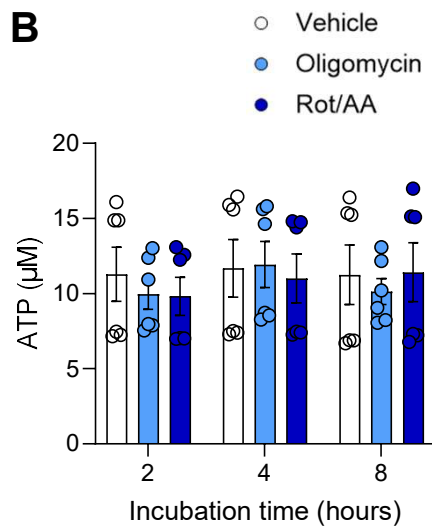
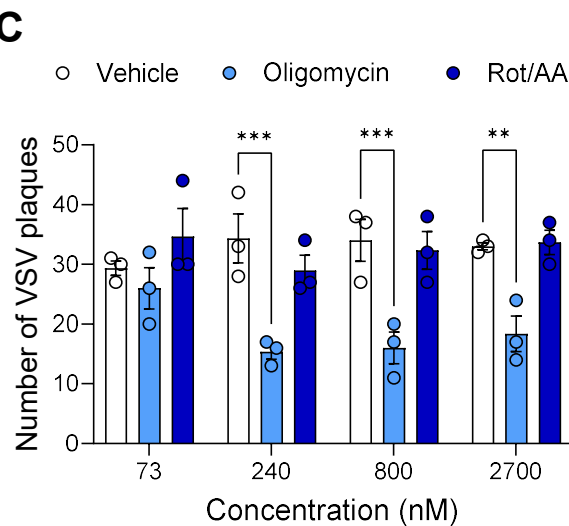
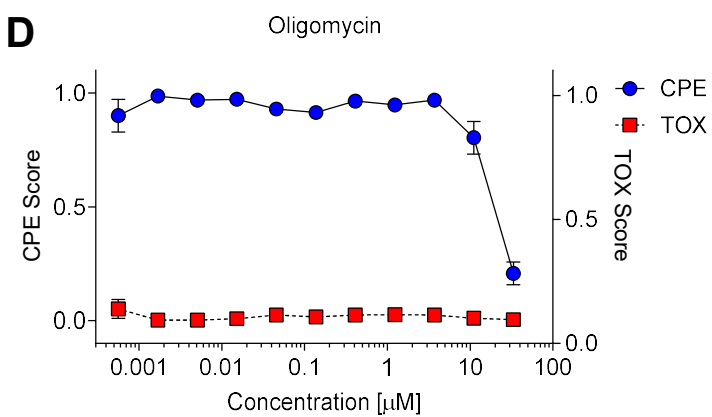
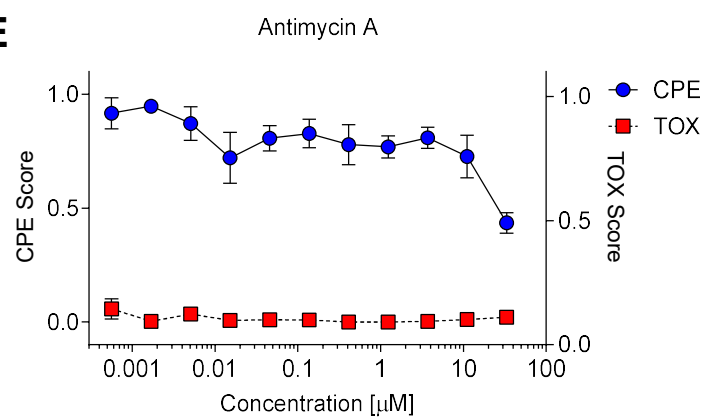
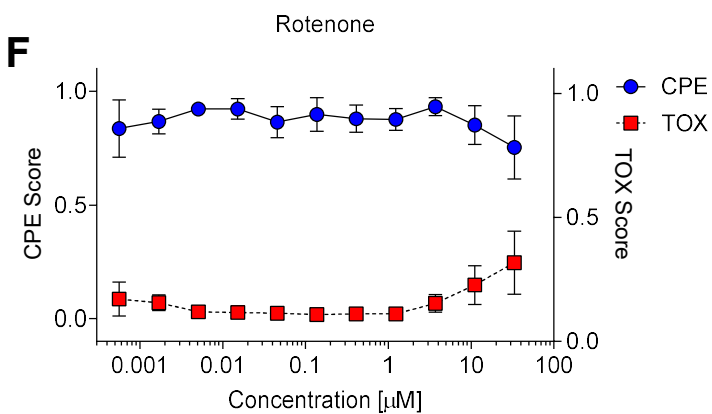
**Figure S1: Supplemental information for the single cell RNA sequencing and ETC gene expression after viral infection, related to Figure 1.**

(A) VSV infected cells were stained with anti-VSV glycoprotein antibody (Vi-10) at 24h post-infection. HEK cells were infected with VSV as described in Figure 1A, and monensin was added at 4h post-infection to halt further viral propagation. The remaining cells of the samples for single cell RNA sequencing were used; n=2 for control, n=3 for VSV infected group.

(B) HEK cells were infected with VSV and viable cells were sorted as described in Figure 1A. Viability of the samples for single cell RNA sequencing was assessed after staining with DAPI.

(C) Heatmap showing expression of VSV transcripts in each cell.

(D-H) HEK cells were infected with VSV, LCMV, ZIKV and HSV at MOI=10, mRNA levels of (D) NDUFA12, (E) NDUFA8, (F) UQCRC1, (G) COX5A and (H) ATP5F1 were measured at the indicated time points; data were from two experiments for naïve and 4h post-infection, and one experiment for 2h and 8h post-infection. *p* values were determined using one-way ANOVA with Dunnett's multiple comparisons test. \**p*<0.05, \*\*\**p*<0.001. Data are represented as mean ± S.E.M.

**A****B****C****D****E****F**

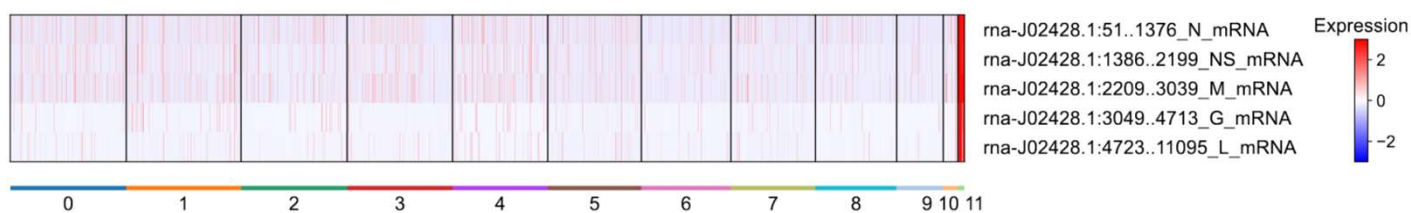
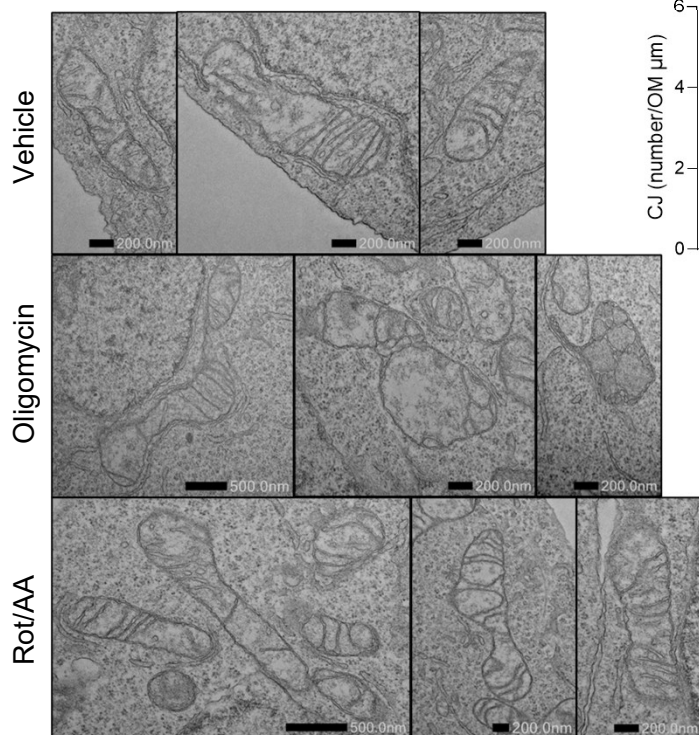
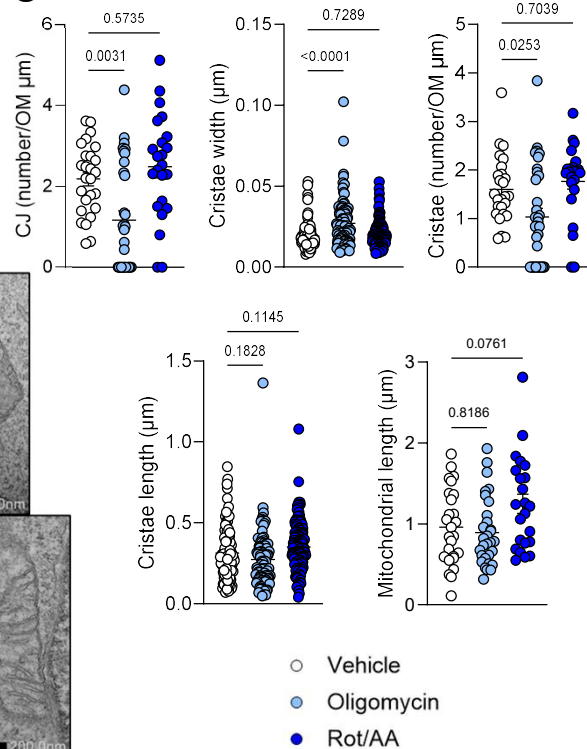
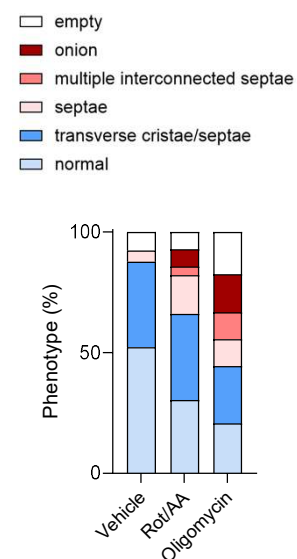
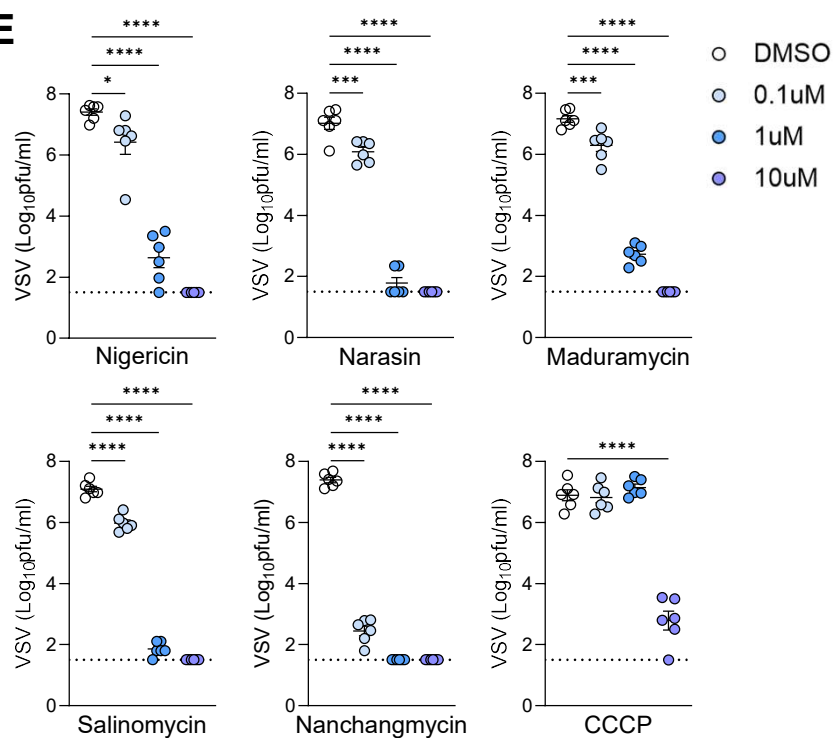
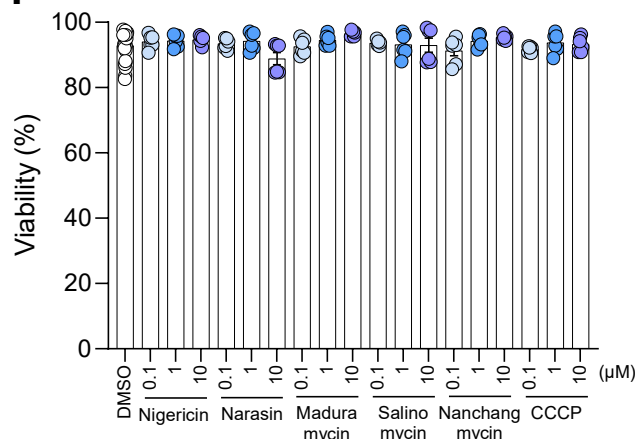
**Figure S2: Oligomycin treatment does not significantly affect early apoptosis or intracellular ATP level. Oligomycin inhibits VSV plaque formation and cytopathic effect of SARS-CoV-2, related to Figure 2.**

(A) Vero cells were treated with 200 nM of oligomycin, 500 nM of rotenone and antimycin or DMSO for 4h or 8h. The treated cells were stained with annexin V and 7AAD; data from two independent experiments are shown. *p* values were determined using ordinary two-way ANOVA with Dunnett's multiple comparisons test. \*\*\*\**p*<0.0001. Data are represented as mean ± S.E.M.

(B) Vero cells were treated with 200 nM of oligomycin, 500 nM of rotenone and antimycin or DMSO for 2h, 4h or 8h. The treated cells were lysed after washing with PBS and ATP concentration was quantified with Luminescent ATP Detection Assay Kit; data from two independent experiments are shown. Statistical significance was determined by ordinary two-way ANOVA with Dunnett's multiple comparisons test. Data are represented as mean ± S.E.M.

(C) VSV plaque formation in Vero cells pre-treated with oligomycin, Rot/AA or vehicle; data were from one experiment pooled with n=3. *p* values were determined using ordinary two-way ANOVA with Dunnett's multiple comparisons test. \*\**p*<0.01, \*\*\**p*<0.001. Data are represented as mean ± S.E.M.

(D-F) Vero cells were treated with the indicated concentration of (D) oligomycin, (E) antimycin and (F) rotenone for 20 min prior to infection with SARS-CoV-2 at MOI of 0.03. Images were taken 3 days post-infection and CPE scores (blue) and TOX scores (red) were determined by 'CPETOXnet' and are shown in a concentration-dependent manner; data from two independent experiments are shown.

**A****B****C****D****E****F**

**Figure S3: Rot/AA treatment has only modest effect on cristae structure and mitochondrial morphology compared to oligomycin. Uncouplers reduce VSV replication without significantly affecting cell viability, related to Figure 3.**

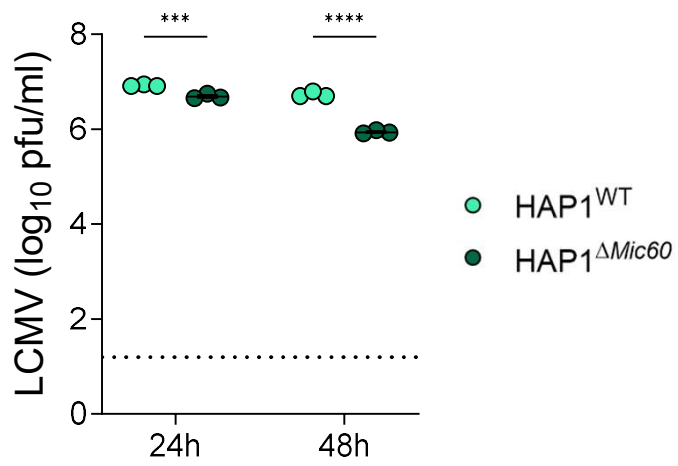
(A) Heatmap showing expression of VSV transcripts in each cell. The numbers at the bottom refer to the cluster numbers.

(B-D) HAP1 cells were treated with 200 nM of oligomycin, 500 nM of Rot/AA or vehicle for 8h. (B) Representative transmission electron microscopy (TEM) micrographs. Scale bar lengths are specified individually on each image: the scale bar in the left panel of oligomycin and Rot/AA represents 500nm, while all other scale bars indicate 200nm. (C) Quantification of TEM micrographs: number of crista junction, cristae length, cristae width, number of cristae and mitochondrial length were analyzed; 23-30 mitochondria per condition were analyzed. Statistical significance was determined using one-way ANOVA with Dunnett's multiple comparisons test. Data are represented as mean  $\pm$  S.E.M. (D) Mitochondria were classified based on morphological phenotype and relative abundance is shown; 56-65 mitochondria per condition were analysed.

(E) Vero cells were infected with VSV at MOI=0.001 after the pre-treatment with the indicated uncouplers for 30 min. VSV titers in the supernatant were quantified at 16h post-infection; data are representative of two independent experiments.  $p$  values were determined using one-way ANOVA with Dunnett's multiple comparisons test. \* $p$ <0.05, \*\*\* $p$ <0.001, \*\*\*\* $p$ <0.0001. Data are represented as mean  $\pm$  S.E.M.

(F) Vero cells were treated with the compounds at the indicated concentrations for 16 hours. The relative abundance of annexin V-/ 7AAD<sup>-</sup> cells is shown as viability: data are representative of two experiments. Statistical significance was determined by one-way ANOVA with Dunnett's multiple comparisons test. Data are represented as mean  $\pm$  S.E.M.



**A**

**Figure S4: LCMV replication is reduced in MIC60 deficient HAP1 cells, related to Figure 4.**

(A) WT and MIC60-deficient HAP1 cells were infected with LCMV WE at MOI=1. LCMV titer in the infected supernatant was measured at the indicated time points; data from one experiment pooled with n=3 per condition are shown. Significance was determined using ordinary two-way ANOVA followed by Sidak's multiple comparisons test. \*\*\* $p < 0.001$ , \*\*\*\* $p < 0.0001$ . Data are represented as mean  $\pm$  S.E.M.

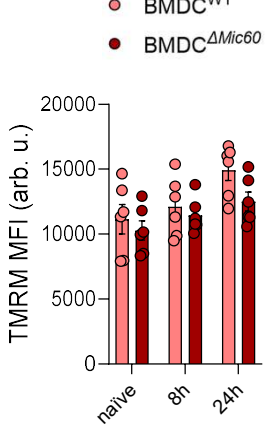
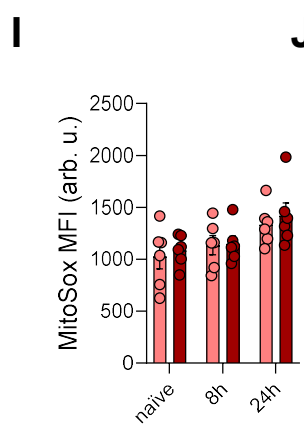
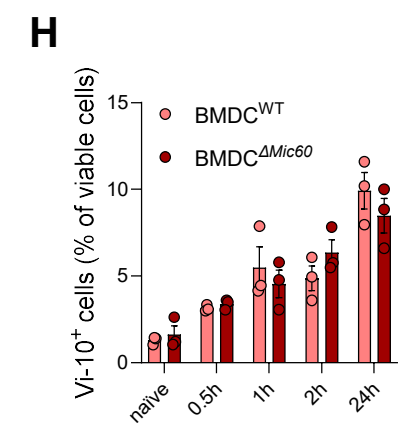
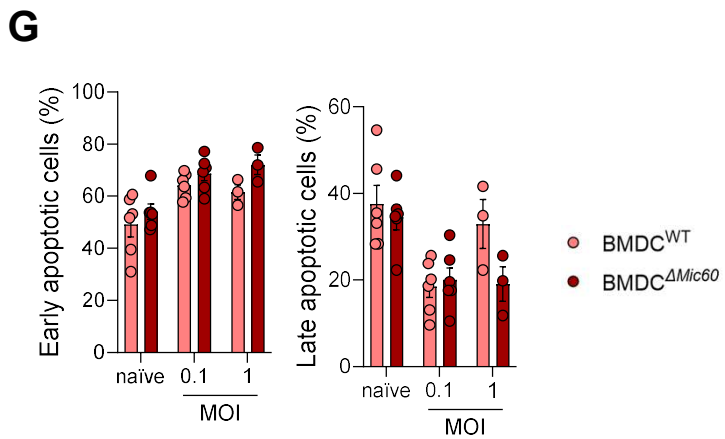
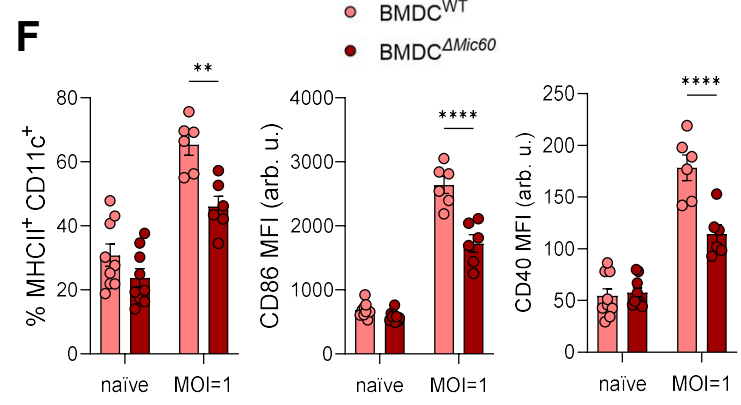
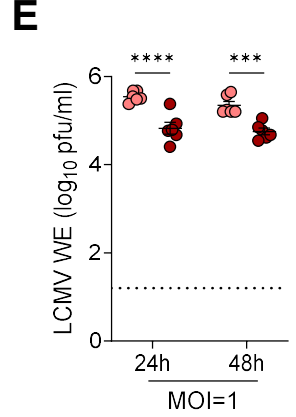
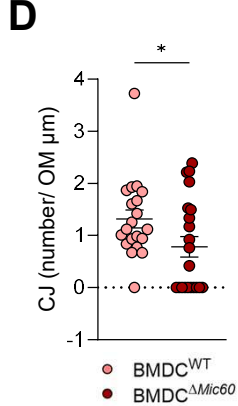
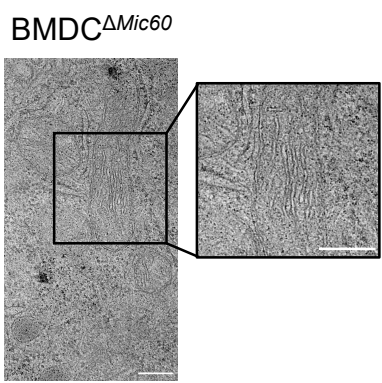
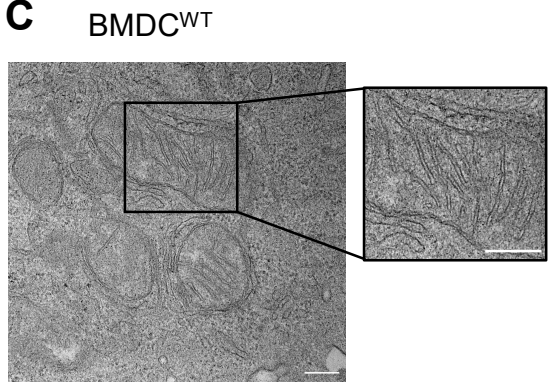
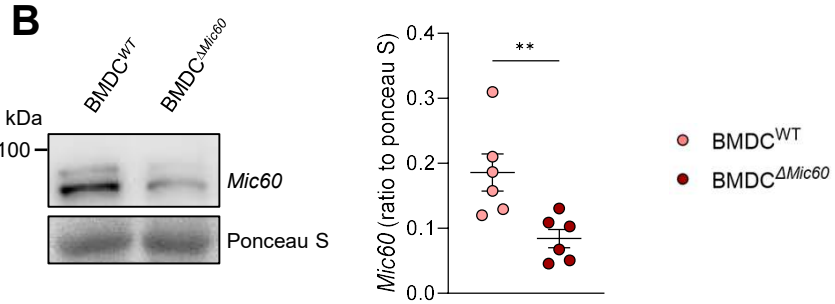
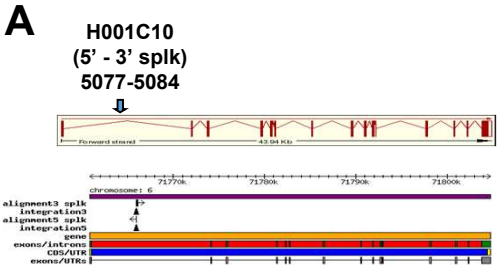


**Figure S5: Supplemental information for generation of *Mic60*<sup>inv/inv</sup> × *CD11c-Cre*<sup>+</sup> mice, and characterization of MIC60 deficient BMDCs, related to Figure 5.**

(A) Schematics of IMMT<sup>GT(H001C10)WRST</sup>:MGI:3897023, where the gene trap had inserted in the intron 1 of the *Mic60* (*IMMT*) gene locus.

(B) MIC60 expression in BMDCs from WT or *Mic60*<sup>inv/inv</sup> × *CD11c-Cre*<sup>+</sup> mice; data from two independent experiments pooled with n=6 mice per condition are shown. Significance was determined using two-tailed/unpaired Student's t-test. \*\**p*<0.01. Data are represented as mean ± S.E.M.

(C) Representative TEM micrographs of MIC60-deficient and competent BMDCs and (D) quantification of CJs; scale bar 200 nm, data from two experiments pooled with n=2 mice per condition. Significance was determined by two-tailed/unpaired Student's t-test. \**p*<0.05. Data are represented as mean ± S.E.M.

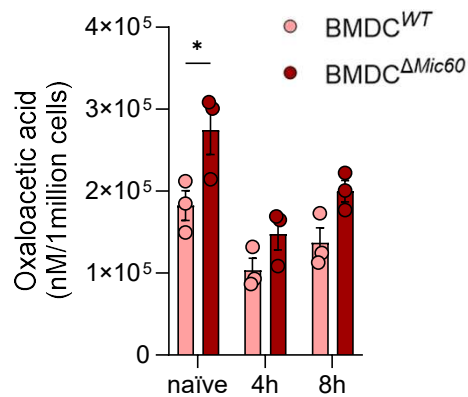
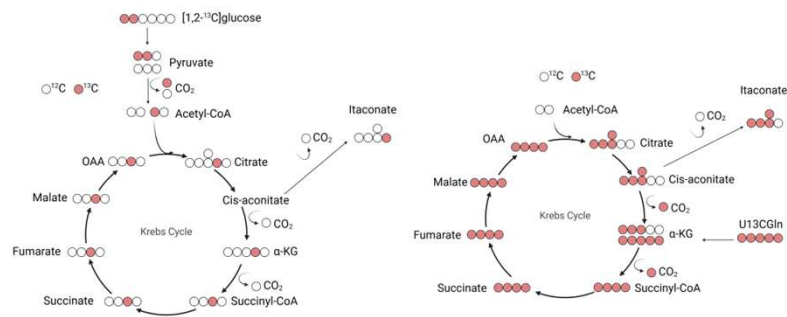
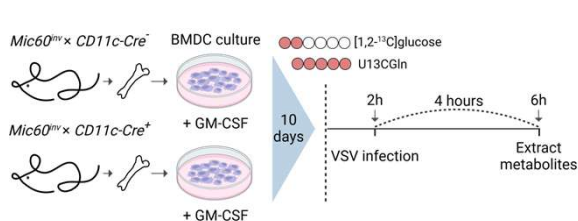
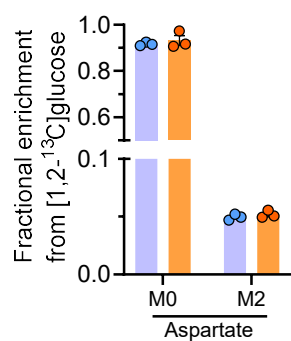
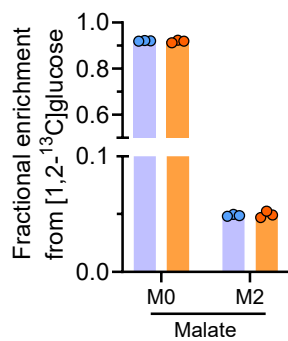
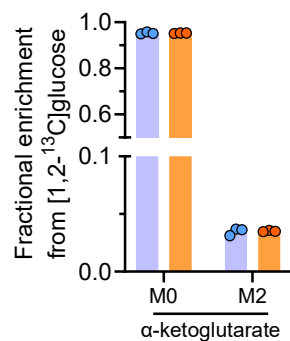
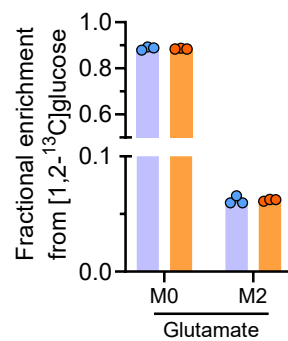
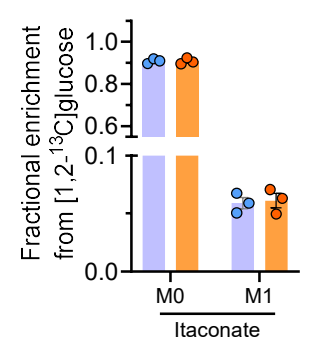
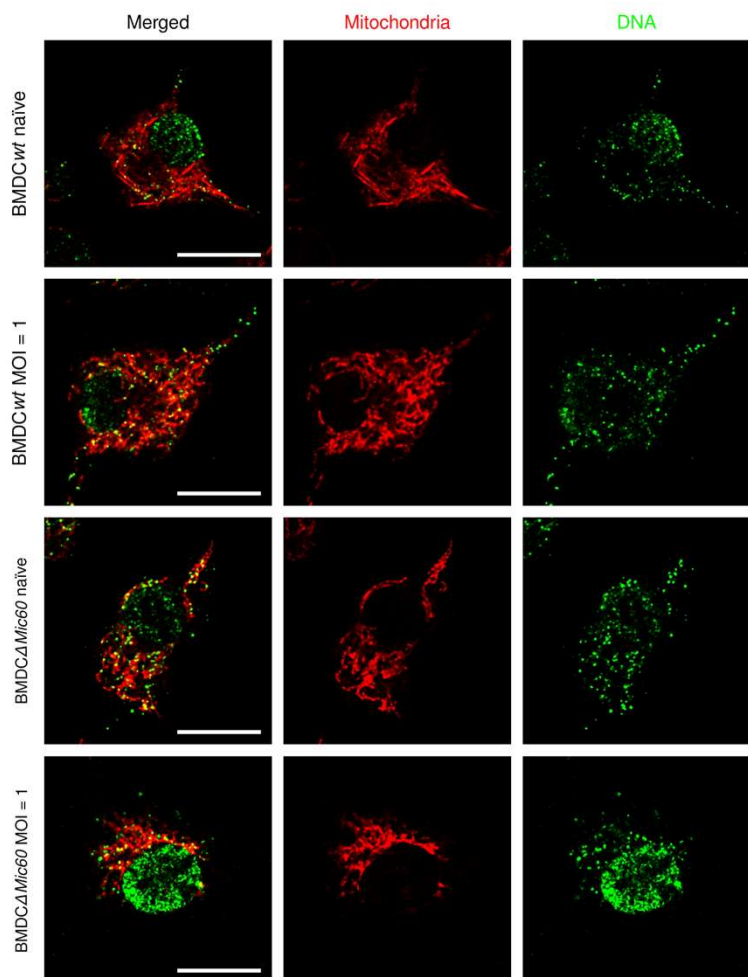
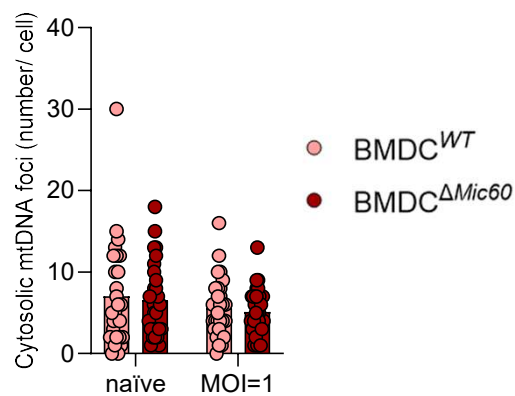
(E) MIC60-deficient and competent BMDCs were infected with LCMV WE strain at MOI=1. LCMV titer in the infected supernatant was measured at the indicated time points; data from two independent experiments pooled with n=6 mice. *p* values were determined using ordinary two-way ANOVA followed by Sidak's multiple comparisons test. \*\*\**p*<0.001, \*\*\*\**p*<0.0001. Data are represented as mean ± S.E.M.

(F) Statistics of CD11c<sup>+</sup>MHC-II<sup>+</sup> BMDCs, MFI of CD86 and CD40 related to Figure 5G-I; data from three experiments pooled with n=9 mice for naïve condition and two experiments pooled with n=6 mice for infected condition. Significance was determined using ordinary two-way ANOVA followed by Sidak's multiple comparisons test. \*\**p*<0.01, \*\*\*\**p*<0.0001. Data are represented as mean ± S.E.M.

(G) BMDCs were infected with VSV at indicated MOI and the cells were stained with annexin V and 7AAD at 24h post-infection; data are representative of six biological replicates for naïve and MOI=0.1 and three biological replicates for MOI=1 condition. Significance was analyzed using ordinary two-way ANOVA followed by Sidak's multiple comparisons test. Data are represented as mean ± S.E.M.

(H) BMDCs were infected with VSV at MOI=1 and monensin was added at indicated time points to halt further entry of viral particles. The cells were stained with Vi-10 at 24h post-infection; data represent three biological replicates. Significance was analyzed by ordinary two-way ANOVA followed by Sidak's multiple comparisons test. Data are represented as mean ± S.E.M.

(I-J) BMDCs were infected with VSV at MOI=0.1 and at 8 and 24h post-infection, the cells were stained with (I) MitoSox and (J) TMRM; data were from two independent experiments pooled with n=6 mice. Statistical significance was analyzed using ordinary two-way ANOVA followed by Sidak's multiple comparisons test. Data are represented as mean ± S.E.M.

**A****B****C****D****E****F****G****H****I****J**

**Figure S6: Metabolic flux analysis and cytosolic mtDNA quantification in MIC60-competent or deficient BMDCs, related to Figure 6**

(A) statistics of oxaloacetic acid concentration in MIC60-competent or deficient BMDCs, related to Figure 6E; data are representative of three biological replicates. Significance was determined using ordinary two-way ANOVA followed by Sidak's multiple comparisons test. \* $p < 0.05$ . Data are represented as mean  $\pm$  S.E.M.

(B) Fluxmap of mammalian central carbon metabolism; illustration was created with Biorender.com.

(C) Schematic depicting experimental procedures of metabolic flux analysis in BMDCs; illustration was made with Biorender.com.

(D-H) MIDs (mass isotopomer distributions) of (D) aspartate, (E) malate, (F)  $\alpha$ -ketoglutarate, (G) glutamate and (H) itaconate from MIC60-competent or deficient BMDCs that were incubated with [1,2- $^{13}\text{C}$ ] glucose; data are representative of three biological replicates. Data are represented as mean  $\pm$  S.E.M.

(I-J) Quantification of cytosol DNA foci released from mitochondria. BMDCs were infected with VSV at MOI=1 for 4h. Cytosolic DNA foci were counted manually when cytosolic DNA foci are not co-localized with mitochondria; scale bar 10 $\mu\text{m}$ , data are representative of three biological replicates, 30 cells per condition were analyzed except naïve WT BMDCs (27 cells). Statistical significance was analyzed using ordinary two-way ANOVA followed by Sidak's multiple comparisons test. Data are represented as mean  $\pm$  S.E.M.



**Table S1: Primers for real-time quantitative PCR**

Gene	Forward Primer	Reverse Primer
VSV glycoprotein	5'-ACGGCGTACTTCCAGATGG-3'	5'-CTCGGTTCAAGATCCAGGT-3'
Gapdh mouse	5'-ACAAC TTTGGTATCGTGGAAGG-3'	5'-GCCATCACGCCACAGTTTC-3'
Ifnb1 mouse	5'-CAGCTCCAAGAAAGGACGAAC-3'	5'-GGCAGTGTA ACTCTTCTGCAT-3'
Ifna4 mouse	5'-TGATGAGCTACTACTGGTCAGC-3'	5'-GATCTCTTAGCACAAAGGATGGC-3'
Cxcl10 mouse	5'-CCAAGTGCTGCCGTCATTTTC-3'	5'-GGCTCGCAGGGATGATTCAA-3'
ND6 human	5'-GCGATGGCTATTGAGGAGTATCC-3'	5'-CACAGCACCAATCCTACCTCCA-3'
MT-CO1 human	5'-TCTCAGGCTACACCCTAGACCA-3'	5'-ATCGGGGTAGTCCGAGTAACGT-3'
Mx1 mouse	5'-GACCATAGGGGTCTTGACCAA-3'	5'-AGACTTGCTCTTTCTGAAAAGCC-3'
Ifit2 mouse	5'-AGTACAACGAGTAAGGAGTCACT-3'	5'-AGGCCAGTATGTTGCACATGG-3'
Ifit3 mouse	5'-CCTACATAAAGCACCTAGATGGC-3'	5'-ATGTGATAGTAGATCCAGGCGT-3'
NDUFA12 human	5'-GGTCTCCGAGGCTATCTACGG-3'	5'-GGAGGCACCATGCTTCCATC-3'
NDUFA8 human	5'-CCCAACAAGGAGTTTATGCTCT-3'	5'-CACAGTGACGTTTTATCTGCCT-3'
UQC RFS1 human	5'-CTGAATACCGCCGCCTTGAA-3'	5'-ATGCGACACCCACAGTAGTTA-3'
COX5A human	5'-ATCCAGTCAGTTCGCTGCTAT-3'	5'-CCAGGCATCTATATCTGGCTTG-3'
ATP5F1 human	5'-AGGTCCAGGGGTATTGCAG-3'	5'-TCCTCAGGGATCAGTCCATAAC-3'